



## Thermotropic phase boundaries in classic ferroelectrics

Lummen, T. T. A., Gu, Y., Wang, J., Lei, S., Xue, F., Kumar, A., Barnes, A. T., Barnes, E., Denev, S., Belianinov, A., Holt, M., Morozovska, A. N., Kalinin, S. V., Chen, L.-Q., & Gopalan, V. (2014). Thermotropic phase boundaries in classic ferroelectrics. *Nature Communications*, 5, Article 3172.  
<https://doi.org/10.1038/ncomms4172>

**Published in:**  
Nature Communications

**Document Version:**  
Peer reviewed version

**Queen's University Belfast - Research Portal:**  
[Link to publication record in Queen's University Belfast Research Portal](#)

**Publisher rights**  
Copyright 2014 Macmillan Publishers Limited. All rights reserved.

**General rights**  
Copyright for the publications made accessible via the Queen's University Belfast Research Portal is retained by the author(s) and / or other copyright owners and it is a condition of accessing these publications that users recognise and abide by the legal requirements associated with these rights.

**Take down policy**  
The Research Portal is Queen's institutional repository that provides access to Queen's research output. Every effort has been made to ensure that content in the Research Portal does not infringe any person's rights, or applicable UK laws. If you discover content in the Research Portal that you believe breaches copyright or violates any law, please contact [openaccess@qub.ac.uk](mailto:openaccess@qub.ac.uk).

**Open Access**  
This research has been made openly available by Queen's academics and its Open Research team. We would love to hear how access to this research benefits you. – Share your feedback with us: <http://go.qub.ac.uk/oa-feedback>

## **Thermotropic Phase Boundaries in Classic Ferroelectrics**

Tom. T.A. Lummen<sup>1</sup>, Yijia Gu<sup>1</sup>, Jianjun Wang<sup>1,2</sup>, Shiming Lei<sup>1</sup>, Fei Xue<sup>1</sup>, Amit Kumar<sup>1,3</sup>, Andrew T. Barnes<sup>1</sup>, Eftihia Barnes<sup>1</sup>, Sava Denev<sup>1</sup>, Alex Belianinov<sup>3</sup>, Martin Holt<sup>4</sup>, Anna N. Morozovska<sup>5</sup>, Sergei V. Kalinin<sup>3</sup>, Long-Qing Chen<sup>1</sup> & Venkatraman Gopalan<sup>1,\*</sup>

<sup>1</sup>*Department of Materials Science and Engineering, Pennsylvania State University, University Park, Pennsylvania 16802, USA*

<sup>2</sup>*Department of Physics, University of Science and Technology Beijing, Beijing 100083, China*

<sup>3</sup>*Center for Nanophase Materials Sciences, Oak Ridge National Laboratory, Oak Ridge, Tennessee 37831, USA*

<sup>4</sup>*Center for Nanoscale Materials, Argonne National Laboratory, Argonne, IL 60439, USA*

<sup>5</sup>*Institute of Physics, National Academy of Sciences of Ukraine, 46, Nauki, 03028 Kiev, Ukraine*

\*Correspondence should be addressed to V.G. ([vxg8@psu.edu](mailto:vxg8@psu.edu)).

**High performance piezoelectrics are lead-based solid-solutions that exhibit a so-called morphotropic phase boundary (MPB), which separates two competing phases as a function of chemical composition; as a consequence, an intermediate low-symmetry phase with a strong piezoelectric effect arises. In search for environmentally sustainable lead-free alternatives that exhibit analogous characteristics, we use a network of competing domains to create similar conditions across thermal inter-ferroelectric transitions in simple, lead-free ferroelectrics such as BaTiO<sub>3</sub> and KNbO<sub>3</sub>. Here, we report the experimental observation of thermotropic phase boundaries (TPBs) in these classic ferroelectrics, through direct imaging of low-symmetry intermediate phases that exhibit large enhancements in the existing nonlinear optical and piezoelectric property coefficients. Furthermore, the symmetry**

**lowering in these phases allows for new property coefficients that exceed all the existing coefficients in both parent phases. Discovering the thermotropic nature of thermal phase transitions in simple ferroelectrics thus presents unique opportunities for the design of ‘green’ high-performance materials.**

High-performance piezoelectric materials are pivotal to modern day ‘smart’ technologies that integrate ultra-sensitive sensing and high-precision actuation functions in biomedical devices, telecommunications and scientific research<sup>1,2</sup>. Typically, such smart materials are complex lead-based solid solutions that exhibit a so-called morphotropic phase boundary (MPB); a compositional region separating two competing ferroelectric phases, where an intermediate phase with strongly enhanced functional properties arises<sup>3-6</sup>. To develop viable alternatives to lead-based piezoelectrics, systems that mimic the principal characteristics<sup>5-8</sup> of morphotropic phase boundaries (MPBs) have been pursued by means of composition<sup>9,10</sup>, pressure<sup>11</sup>, epitaxial strain<sup>12,13</sup>, multilayering<sup>14,15</sup> and domain microstructure<sup>16-18</sup>. In classic lead-free materials such as BaTiO<sub>3</sub> and KNbO<sub>3</sub> for example, creating frustrated ferroelectric domains by external fields has been shown to substantially enhance piezoelectric response<sup>16,17</sup>. However, the exact mechanism of this phenomenon has been the subject of extensive debate in recent years<sup>19-27</sup>; the possible existence of a monoclinic phase in BaTiO<sub>3</sub> single crystals has been reported<sup>25,28-29</sup>, but it has never been directly imaged on a microscopic level. As a result, the important question of whether the observed phase is of *intrinsic* monoclinic symmetry, or in fact corresponds to a symmetry-adaptive superlattice of nano-domains<sup>21,30-37</sup> (such as those observed in MPBs) remains open. Here we use the mutual interactions inherent to a network of competing domains to create MPB-like conditions across thermal ferroelectric transitions in simple, lead-free ferroelectrics. We provide direct experimental evidence of the resulting intermediate phases of *intrinsic* monoclinic symmetry using several complementary imaging techniques, while simultaneously mapping their enhanced nonlinear optical and piezoelectric properties on the nanoscale. Thus, we reveal the *thermotropic* character of thermal ferroelectric phase transitions in classic ferroelectrics. The rationale for this terminology is two-fold. On the one hand it draws the analogy to MPBs while emphasizing that here we

consider thermal ('*thermo*-') instead of compositional ('*morpho*-') phase boundaries. On the other hand it underlines the similarity to the physics of thermotropic liquid crystals, which exhibit different types of liquid-like orientational order ('-*tropos*') in a certain temperature range<sup>38</sup>. In the following, we focus on the well-known BaTiO<sub>3</sub> and KNbO<sub>3</sub> as representative examples of simple, lead-free ferroelectrics.

## Results

**Thermotropic phase boundaries.** In the bulk, *single domain* case, both these perovskite systems undergo a series of first-order ferroelectric transitions upon heating, sequentially adopting rhombohedral (R), orthorhombic (O) and tetragonal (T) ferroelectric phases before reverting to the cubic parent phase (C). In *multi-domain* configurations however, phase-field simulations predict the emergence of an intermediate phase if sufficient competing mechanical and dipolar interactions between domains exist. Figure 1a shows the temporal evolution of the phase fractions in an orthogonally domain-twinned BaTiO<sub>3</sub> system as it is heated through its O-T phase boundary, calculated using phase-field simulations (see Materials and Methods). As can be seen, these simulations predict the emergence of a kinetically intermediate phase of monoclinic (M<sub>C</sub>) symmetry<sup>39</sup> which is defined by a spontaneous ferroelectric polarization ( $\mathbf{P}_s$ ) that significantly deviates ( $>5^\circ$ ) from the corresponding T and O directions. Moreover, as shown in Figure 1b, this M<sub>C</sub> phase is thermodynamically stabilized in significant volume fractions (20-60%) over a wide temperature range of over 100 K. This intriguing reduction of the polar anisotropy<sup>40</sup> is illustrated by the domain structure in Figure 1c, which reveals a persistent network of bulk M<sub>C</sub> regions at room temperature (298 K). The thermotropic character of the ferroelectric phase boundary originates from the in-plane shear stress ( $\sigma_{23}$ ) and transverse electric field ( $E_2$ ) components that

are inherently generated by the orthogonal in-plane domain twins (see Supplementary Discussion 1 and Supplementary Figure 1).

To experimentally confirm the thermotropic nature of ferroelectric phase boundaries, we investigate the local symmetry, microscopic structure and properties of these intermediate phases through a variety of complementary nanoscale imaging techniques.

**Symmetry and nonlinear optical properties.** Considering that both ferroelectricity and piezoelectricity only occur in materials that lack a structural center of inversion, we employ nonlinear optical Second Harmonic Generation (SHG) — a second order process that requires the same lack of inversion symmetry<sup>41,42</sup> — to image and assess the local symmetry in these systems. Figure 2 compares scanning SHG microscopy images of a BaTiO<sub>3</sub> single crystal in selected areas *with* and *without* orthogonal domain twinning. The domain structure in Figure 2a, comprised of only a single set of parallel 90° twin walls, exhibits the typical bright-dark SHG contrast corresponding to in-plane tetragonal *a* and *b* domains. As confirmed using spatially resolved SHG polarimetry, their SHG signature seems to adhere perfectly to the nominal tetragonal symmetry of point group *4mm* (Supplementary Figure 2). In contrast, the competition between the two sets of orthogonal twin domains in Figure 2b induces the anticipated intermediate M<sub>C</sub> phase, which is characterized by a ‘staircase’ pattern and meandering ripples of strongly enhanced SHG intensity. Local symmetry analysis through SHG polarimetry, Figure 2c, shows that the point group symmetry in this phase is indeed monoclinic (point group *m*), as expected for an M<sub>C</sub> phase. Independently, this is also confirmed using complementary spatially resolved micro-Raman microscopy (see Supplementary Figure 3). Since the only symmetry element in this point group—the *m* mirror plane—is parallel to the surface of the crystal, the ferroelectric polarization in the M<sub>C</sub>

phase is symmetry-allowed to continuously rotate in-plane<sup>3,4,7,11,43</sup>. In this sense, the bridging M<sub>C</sub> phase can be regarded as an analogue of a ‘viscous’ two-dimensional polar liquid, with the rotational degree of freedom illustrated by meandering polarization directions.

This same degree of freedom is responsible for the observed enhancement of the nonlinear optical coefficients. Depending on the experimental configuration, the SHG scans nominally probe the  $d_{32}$  and  $d_{33}$  components of the nonlinear optical tensor of tetragonal BaTiO<sub>3</sub> (see Fig. 2d). By comparison, in the M<sub>C</sub> phase, the SHG intensity is found to reach relative values of up to 1,760%, and effective coefficient enhancements of up to 4.2× and 4.4× are seen for  $d_{32}$  (to  $\approx 89$  pm V<sup>-1</sup>) and  $d_{33}$  (to  $\approx 32$  pm V<sup>-1</sup>), respectively (see Materials and Methods). Moreover, as illustrated in Figure 2, the symmetry lowering to point group  $m$  results in additional large nonzero nonlinear optical coefficients (Fig. 2d), which are neither expected nor observed in tetragonal domains:  $d_{22} \approx 18$  pm V<sup>-1</sup> and  $d_{23} \approx 22$  pm V<sup>-1</sup>.

We have reproducibly observed the M<sub>C</sub> phase at room temperature in various BaTiO<sub>3</sub> single crystals from different sources, both before and after annealing at 1150 K and before and after thermal cycling through the O-T phase boundary. Empirically, it is readily observed whenever orthogonally twinned domain structures are present. Furthermore, an analogous monoclinic phase exhibiting similar SHG enhancements is observed in strongly twinned KNbO<sub>3</sub> single crystals at room temperature (Supplementary Figure 4), which underscores the generality of the concept of thermotropic phase boundaries in ferroelectrics. In contrast to tetragonal BaTiO<sub>3</sub>, KNbO<sub>3</sub> is nominally orthorhombic at ambient temperatures, where it is situated closest to the R-O phase boundary.

**Structure.** There are prior reports of an intermediate M<sub>C</sub> phase near the thermal O-T phase

boundary of BaTiO<sub>3</sub>. Cao *et al.* reported on a M<sub>C</sub> phase at 265 K, discovered after cooling BaTiO<sub>3</sub> single crystals through the T-O transition under an applied electric field<sup>28</sup>. Recently, Eisenschmidt *et al.* observed monoclinic M<sub>C</sub>-type short range order while slowly cooling BaTiO<sub>3</sub> single crystals through the same transition<sup>29</sup>. However, both these works employed conventional x-ray diffraction techniques, wherein many ferroelectric domains are probed simultaneously due to the large size of the x-ray beam. As a result, neither work could experimentally determine whether the observed low-symmetry stems from an *intrinsically* monoclinic structure, or from a domain-averaged adaptive superlattice consisting of nanotwinned parent-phase domains<sup>21,30-37</sup> (Supplementary Discussion 2.1). Here we experimentally demonstrate the natural occurrence of a bulk, long-range ordered M<sub>C</sub> phase in unpoled BaTiO<sub>3</sub> at room temperature; at considerable distance from the thermal O-T phase boundary. Moreover, by employing a state-of-the-art focused beam diffraction technique, Scanning X-ray Diffraction Microscopy (nano-SXDM<sup>44,45</sup>), we show below that the observed M<sub>C</sub> phase is an *intrinsically* monoclinic structure, as opposed to a consequence of hypothetical nanoscale domain twinning.

Nanoscale SXDM measurements reveal that the (220) diffraction corresponding to the M<sub>C</sub> structure appears as a newly observed peak close to the (220) diffraction peak of tetragonal *b* domains (Fig. 3a-c). Due to the intentional shadowing of the focused beam center in SXDM, each Bragg diffraction peak typically appears as two vertically separated lobes, whose angular center of mass (COM) reflects the corresponding ( $2\theta, \chi$ ) coordinate (Supplementary Figure 5)<sup>44,45</sup>. The extended area diffraction image in Figure 3a demonstrates that the observed M<sub>C</sub> diffraction cannot be due to conventional diffraction from coarse tetragonal or orthorhombic domain twins, as any such reflection would fall well outside of the experimental zoom-in window used throughout our imaging experiments (see also Supplementary Discussion 2.2). Moreover, a possible nanotwinning

origin can be ruled out as unphysical, as the position of the  $M_C$  diffraction peak violates both the reciprocal space lever rule<sup>35-37</sup> (Figure 3d and Supplementary Figures 6-8) as well as the general invariance conditions<sup>31-33</sup> of any potential adaptive phase. In addition, both theory<sup>46,47</sup> and experiment<sup>48-53</sup> demonstrate that the crucial requirement for adaptive phase formation, an extremely low domain wall energy<sup>31,32,54</sup>, does not apply in  $\text{BaTiO}_3$  at 298 K (Supplementary Figures 9-10). For an in-depth discussion on the exclusion of nanotwinned adaptive phases, see Supplementary Discussion 2.3.

Instead, the (220)  $M_C$  diffraction is consistent with a simple shear distortion of the tetragonal unit cell that reduces the symmetry to point group  $m$  (inset Fig. 3d). An SXDM rocking curve analysis determines the typical shear angle  $|\delta_M|$  to be  $\sim 0.018^\circ$ , clearly identifying the  $M_C$  structure as an intermediate phase that bridges the purely tetragonal ( $|\delta_T| = 0^\circ$ ) and orthorhombic ( $|\delta_O| = 0.075^\circ$ ) structures<sup>29</sup> (see Supplementary Discussion 3 and Supplementary Figures 11-12). Comparing a spatial map of the integrated intensity of the  $M_C$  peak (Fig. 3e) to the complementary scanning SHG image in the same area (Fig. 3f) clearly shows their close correspondence, consolidating the monoclinic origin of the  $M_C$  diffraction. Furthermore, the micron-scale spatial variation of its  $2\theta$  position (shown in Figure 3g and Supplementary Figure 12c) indicates micron-scale continuous changes of the magnitude and sign of the shear angle  $\delta_M$  within the  $M_C$  staircase pattern, most likely related to the meandering bright-dark SHG ripples observed in Figure 2. We note that  $\delta_M$  does not directly correspond to the rotation of the ferroelectric polarization, which can lie anywhere within the sheared mirror plane.

**Piezoelectric properties.** Since the piezoelectric properties near the thermotropic phase boundaries are of specific interest, we measure the local piezoresponse of the  $M_C$  phase in

orthogonally twinned BaTiO<sub>3</sub> (Fig. 4)<sup>55</sup>. As anticipated, both the amplitude (Fig. 4a) and phase (Fig. 4b) of the piezoresponse in the M<sub>C</sub> phase are clearly distinct from those in tetragonal BaTiO<sub>3</sub>, which is evident from a comparison with the corresponding scanning SHG image (Fig. 4c). Due to the in-plane domain geometry, the measured vertical piezoresponse corresponds to the voltage-induced *in-plane* displacement of the sample surface (Supplementary Discussion 4). As illustrated by the inset in Fig 4a, a large piezoelectric displacement is induced in the *a*-domains of the M<sub>C</sub> phase, which is entirely absent in the adjacent tetragonal *a*-domains. This is in excellent agreement with combined phase-field and finite element modeling, which show that this *effective* displacement arises from a combination of newly induced  $d_{16}$  and  $d_{22}$  coefficients (Supplementary Figure 13). As shown in Figure 4d, all the piezoelectric  $d_{ij}$  coefficients are strongly dependent on the ferroelectric polarization angle,  $\beta$ . For example, by combining experimental and simulation data, we estimate a monoclinic polarization angle of  $\beta \approx 17^\circ$  in position 1 of the experimentally observed M<sub>C</sub> phase, with corresponding values of  $d_{16} \approx 69 \text{ pm V}^{-1}$  and  $d_{22} \approx 500 \text{ pm V}^{-1}$  (Supplementary Figure 13d). For optimum polarization angles in the M<sub>C</sub> phase ( $\beta \approx 25^\circ$ ), the piezoelectric  $d_{22}$  coefficient is predicted to peak at  $\approx 840 \text{ pm V}^{-1}$ , which exceeds all existing piezoelectric coefficients of both parent phases.

## Discussion

Our findings reveal that phase transitions in ferroelectrics are intimately coupled to the underlying domain microstructure. Even in lead-free BaTiO<sub>3</sub> and KNbO<sub>3</sub>, classic materials that have been known and studied for over sixty years, we have discovered that domains can lend a thermotropic character to their otherwise well-known phase transitions. This leads to the emergence of

intermediate monoclinic phases in a wide temperature range around the conventional ferroelectric transitions. As this phenomenon arises due to the mechanical and dipolar interactions between competing ferroelectric-ferroelastic domains in a complex domain microstructure, advanced nanoscale-resolved multi-technique measurements in the same spatial location, such as those presented here, are required to properly reveal the underlying physics on a microscopic level. We show that in the stabilized intermediate phases, both the piezoelectric and the nonlinear optical properties can be strongly enhanced, and even newly induced. Since the mechanism of symmetry lowering through stresses and fields is in principle universal to non-triclinic ferroelectric crystal systems, these results suggests a host of possibilities for the design of high-performance phases. A fourfold (4x) enhancement in functional coefficients from a simple shear strain on the order of  $10^{-4}$  indicates that controlled symmetry lowering can indeed be a powerful tool for property enhancement and tuning, and does not necessarily require large strains. In this study, a random domain microstructure is shown to inherently generate such strains, thus stabilizing the monoclinic phase. Theory however shows that similar shear stresses and fields, when applied externally to a single domain system, can also generate such monoclinic phases, along with the concomitant property enhancements. Moreover, since symmetry allows the ferroelectric polarization to lie anywhere within the monoclinic mirror plane,  $m$ , it is easy to reorient the local polarizations in a polydomain monoclinic system with external fields to achieve a “poled” monoclinic domain microstructure. In addition, the piezoelectric tensor of the monoclinic phase enables shear modes that are particularly suitable for shear mode piezoelectric devices<sup>56,57</sup>. Capturing these phenomena using phase field theory opens the door to predictive modeling of enhanced material properties, and enables the optimization of relevant extrinsic factors such as domain distribution, impurity content, and external fields. The fundamental insights presented here will allow for further

exploration of strategies to reliably and reproducibly create these high-performance phases through ‘domain-engineering-by-design’.

## References

- <sup>1</sup> Manbachi, A. & Cobbold, S. C. Development and application of piezoelectric materials for ultrasound generation and detection. *Ultrasound* **19**, 187–196 (2011).
- <sup>2</sup> Uchino, K. *Piezoelectric Actuators and Ultrasonic Motors*. Kluwer Academic Publishers, Norwell, MA, USA (1997). ISBN 0792398114.
- <sup>3</sup> Guo, R. *et al.* Origin of the High Piezoelectric Response in PbZr<sub>1-x</sub>Ti<sub>x</sub>O<sub>3</sub>. *Phys. Rev. Lett.* **84**, 5423-5426 (2000).
- <sup>4</sup> Fu, H. & Cohen, R. E. Polarization rotation mechanism for ultrahigh electromechanical response in single-crystal piezoelectrics. *Nature* **403**, 281-283 (2000).
- <sup>5</sup> Noheda, B. & Cox D. E. Bridging phases at the morphotropic boundaries of lead oxide solid solutions. *Phase Transitions* **79**, 5-20 (2006).
- <sup>6</sup> Viehland, D. Effect of Uniaxial Stress Upon the Electromechanical Properties of Various Piezoelectric Ceramics and Single Crystals. *J. Am. Ceram. Soc.* **89**, 775-785 (2006).
- <sup>7</sup> Noheda, B. *et al.* Stability of the monoclinic phase in the ferroelectric perovskite PbZr<sub>1-x</sub>Ti<sub>x</sub>O<sub>3</sub>. *Phys. Rev. B* **63**, 014103 (2000).
- <sup>8</sup> Noheda, B. *et al.* Tetragonal-to-monoclinic phase transition in a ferroelectric perovskite: The structure of PbZr<sub>0.52</sub>Ti<sub>0.48</sub>O<sub>3</sub>. *Phys. Rev. B* **61**, 8687-8695 (2000).
- <sup>9</sup> Zhang, S.-T. *et al.* Lead-free piezoceramics with giant strain in the system Bi<sub>0.5</sub>Na<sub>0.5</sub>TiO<sub>3</sub>-BaTiO<sub>3</sub>-K<sub>0.5</sub>Na<sub>0.5</sub>NbO<sub>3</sub>. I. Structure and room temperature properties. *J. Appl. Phys.* **103**, 034107 (2008).

<sup>10</sup> Ma, C. Guo, H., Beckmann, S. P. & Tan, X. Creation and Destruction of Morphotropic Phase Boundaries through Electrical Poling: A Case Study of Lead-Free  $(\text{Bi}_{1/2}\text{Na}_{1/2})\text{TiO}_3$ - $\text{BaTiO}_3$  Piezoelectrics. *Phys. Rev. Lett.* **109**, 107602 (2012).

<sup>11</sup> Ahart, M. *et al.* Origin of morphotropic phase boundaries in ferroelectrics. *Nature* **451**, 545-548 (2008).

<sup>12</sup> Diéguez, O. *et al.* *Ab initio* study of the phase diagram of epitaxial  $\text{BaTiO}_3$ . *Phys. Rev. B* **69**, 212101 (2004).

<sup>13</sup> Choi, K. J. *et al.* Enhancement of Ferroelectricity in Strained  $\text{BaTiO}_3$  Thin Films. *Science* **306**, 1005-1009 (2004).

<sup>14</sup> Lee, D. *et al.* Mixed Bloch-Néel-Ising character of 180° ferroelectric domain walls. *Phys. Rev. B* **80**, 060102(R) (2009).

<sup>15</sup> Sinsheimer, J. *et al.* Engineering Polarization Rotation in a Ferroelectric Superlattice. *Phys. Rev. Lett.* **109**, 167601 (2012).

<sup>16</sup> Wada, S., Yako, K., Kakemoto, H., Tsurumi, T. & Kiguchi, T. Enhanced piezoelectric properties of barium titanate single crystals with different engineered-domain sizes. *J. Appl. Phys.* **98**, 014109 (2005).

<sup>17</sup> Wada, S. *et al.* Domain Wall Engineering in Lead-Free Piezoelectric Crystals. *Ferroelectrics* **355**, 37-49 (2007).

<sup>18</sup> Park, S. -E., Wada, S., Cross, L. E. & Shrout, T. R. Crystallographically engineered  $\text{BaTiO}_3$  single crystals for high-performance piezoelectrics. *J. Appl. Phys.* **86**, 2746-2750 (1999).

<sup>19</sup> Ahluwalia, R., Lookman T., Saxena A. & Cao W. Domain-size dependence of piezoelectric properties of ferroelectrics. *Phys. Rev. B* **72**, 014112 (2005).

<sup>20</sup> Rao, W. -F. & Wang, Y. U. Domain wall broadening mechanism for domain size effect on enhanced piezoelectricity in crystallographically engineered ferroelectric single crystals. *Appl. Phys. Lett.* **90**, 041915 (2007).

<sup>21</sup> Hlinka, J., Ondrejkovic, P. & Marton, P. The piezoelectric response of nanotwinned BaTiO<sub>3</sub>. *Nanotechnology* **20**, 105709 (2009).

<sup>22</sup> Xiang, Y., Zhang, R. & Cao, W. Piezoelectric properties of domain engineered barium titanate single crystals with different volume fractions of domain walls. *J. Appl. Phys.* **106**, 064102 (2009).

<sup>23</sup> Sluka, T., Tagantsev, A. K., Damjanovic, D., Gureev, M. & Setter, N. Enhanced electromechanical response of ferroelectrics due to charged domain walls. *Nat. Commun.* **3**, 748 (2012).

<sup>24</sup> Ghosh, D. *et al.* Domain Wall Displacement is the Origin of Superior Permittivity and Piezoelectricity in BaTiO<sub>3</sub> at Intermediate Grain Sizes. *Adv. Funct. Mater.* **2013**, (published online, DOI: 10.1002/adfm.201301913).

<sup>25</sup> Yoshimura, Y., Kojima, A., Tokunaga, N., Tozaki, K. & Koganezawa, T. New finding of coherent hybrid structure of BaTiO<sub>3</sub> single crystal in the room temperature phase. *Physics Letters A* **353**, 250-254 (2006).

<sup>26</sup> Keeble, D. S. & Thomas, P. A. On the tetragonality of the room-temperature ferroelectric phase of barium titanate, BaTiO<sub>3</sub>. *J. Appl. Cryst.* **42**, 480-484 (2009).

<sup>27</sup> Rao, W.-F., Xiao, K.-W., Cheng, T.-L., Zhou, J. E., Wang, Y. U. Control of domain configurations and sizes in crystallographically engineered ferroelectric single crystals: Phase field modeling. *Appl. Phys. Lett.* **97**, 162901 (2010).

<sup>28</sup> Cao, H. *et al.*, Monoclinic *Mc* phase in (001) field cooled BaTiO<sub>3</sub> single crystals. *Appl. Phys. Lett.* **94**, 032901 (2009).

<sup>29</sup> Eisenschmidt, Ch., Langhammer, H. T., Steinhausen, R. & Schmidt, G. Tetragonal-Orthorhombic Phase Transition in Barium Titanate via Monoclinic  $M_C$  Type Symmetry. *Ferroelectrics* **432**, 103-116 (2012).

<sup>30</sup> Viehland, D. Symmetry-adaptive ferroelectric mesostates in oriented  $Pb(BI_{1/3}BII_{2/3})O_3-PbTiO_3$  crystals. *J. Appl. Phys.* **88**, 4794-4806 (2000).

<sup>31</sup> Jin, Y. M. *et al.* Adaptive ferroelectric states in systems with low domain wall energy: Tetragonal microdomains. *J. Appl. Phys.* **94**, 3629-3640 (2003).

<sup>32</sup> Jin, Y. M., Wang, Y. U., Khachaturyan, A. G., Li, J. F. & Viehland, D. Conformal Miniaturization of Domains with Low Domain-Wall Energy: Monoclinic Ferroelectric States near the Morphotropic Phase Boundaries. *Phys. Rev. Lett.* **91**, 197601 (2003).

<sup>33</sup> Wang, Y. U. Three intrinsic relationships of lattice parameters between intermediate monoclinic  $M_C$  and tetragonal phases in ferroelectric  $Pb[(Mg_{1/3}Nb_{2/3})_{1-x}Ti_x]O_3$  and  $Pb[(Zn_{1/3}Nb_{2/3})_{1-x}Ti_x]O_3$  near morphotropic phase boundaries. *Phys. Rev. B* **73**, 014113 (2006).

<sup>34</sup> Schönau, K. A., *et al.* Nanodomain structure of  $Pb[Zr_{1-x}Ti_x]O_3$  at its morphotropic phase boundary: Investigations from local to average structure. *Phys. Rev. B* **75**, 184117 (2007).

<sup>35</sup> Wang, Y. U. Diffraction theory of nanotwin superlattices with low symmetry phase. *Phys. Rev. B* **74**, 104109 (2006).

<sup>36</sup> Wang, Y. U. Diffraction theory of nanotwin superlattices with low symmetry phase: Application to rhombohedral nanotwins and monoclinic  $M_A$  and  $M_B$  phases. *Phys. Rev. B* **76**, 024108 (2007).

<sup>37</sup> Wang, Y. U. Diffraction theory of nanotwin superlattices with low symmetry phase: Adaptive diffraction of imperfect nanotwin superlattices. *Philos. Mag.* **90**, 197-217 (2010).

<sup>38</sup> Kumar, S. *Liquid Crystals – Experimental Study of Physical Properties and Phase Transitions*. Cambridge University Press, Cambridge, UK (2001). ISBN 0521461324.

<sup>39</sup> Vanderbilt, D. & Cohen, M. H. Monoclinic and triclinic phases in higher-order Devonshire theory. *Phys. Rev. B* **63**, 094108 (2001).

<sup>40</sup> Heitmann, A. A. & Rosetti, G. A., Jr. Polar Anisotropy and Inter-Ferroelectric Transitions in Barium Titanate and its Solid Solutions. *Integr. Ferroelectr.* **126**, 155-165 (2011).

<sup>41</sup> Denev, S., Lummen, T. T. A., Barnes, E., Kumar, A. & Gopalan, V. Probing Ferroelectrics Using Optical Second Harmonic Generation. *J. Am. Ceram. Soc.* **94**, 2699-2727 (2011).

<sup>42</sup> Newnham, R. E. *Properties of Materials*, Oxford University Press Inc., New York, NY, USA (2005). ISBN 07167200094.

<sup>43</sup> Bellaiche, L., García, A. & Vanderbilt, D. Finite-Temperature Properties of  $\text{Pb}(\text{Zr}_{1-x}\text{Ti}_x)\text{O}_3$  Alloys from First Principles. *Phys. Rev. Lett.* **84**, 5427-5430 (2000).

<sup>44</sup> Ying, A. *et al.* Modeling of kinematic diffraction from a thin silicon film illuminated by a coherent, focused X-ray nanobeam. *J. Appl. Cryst.* **43**, 587-595 (2010).

<sup>45</sup> Holt, M. *et al.* Nanoscale Hard X-Ray Microscopy Methods for Materials Studies. *Annu. Rev. Mater. Res.* **43**, 183-211 (2013).

<sup>46</sup> Hlinka, J. & Márton, P. Phenomenological model of a 90° domain wall in  $\text{BaTiO}_3$ -type ferroelectrics. *Phys. Rev. B* **74**, 104104 (2006).

<sup>47</sup> Marton, P., Rychetsky, I. & Hlinka, J. Domain walls of ferroelectric  $\text{BaTiO}_3$  within the Ginzburg-Landau-Devonshire phenomenological model. *Phys. Rev. B* **81**, 144125 (2010).

<sup>48</sup> Tanaka, M. & Honjo, G. Electron Optical Studies of Barium Titanate Single Crystal Films. *J. Phys. Soc. Jpn.* **19**, 954-970 (1964).

<sup>49</sup> Dennis, M. D. & Bradt, R. C. Thickness of 90° ferroelectric domain walls in  $(\text{Ba},\text{Pb})\text{TiO}_3$  single crystals. *J. Appl. Phys.* **45**, 1931-1933 (1937).

<sup>50</sup> Zhang, X., Hashimoto, T., & Joy, D. C. Electron holographic study of ferroelectric domain walls.

*Appl. Phys. Lett.* **60**, 784 (1992).

<sup>51</sup> Zhang, X. *et al.* Electron holography techniques for study of ferroelectric domain walls.

*Ultramicroscopy* **51**, 21-30 (1993).

<sup>52</sup> Floquet, N. & Valot, C. Ferroelectric Domain Walls in BaTiO<sub>3</sub>: Structural Wall Model Interpreting Fingerprints in XRPD Diagrams. *Ferroelectrics* **234**, 107-122 (1999).

<sup>53</sup> Eng, L. M. & Güntherodt, H.-J. Scanning Force Microscopy and Near-Field Scanning Optical Microscopy of Ferroelectric and Ferroelastic Domain Walls. *Ferroelectrics* **236**, 35-46 (2000).

<sup>54</sup> Khachaturyan, A. G., Shapiro, S. M. & Semenovskaya, S. Adaptive phase formation in martensitic transformation. *Phys. Rev. B* **43**, 10832-10843 (1991).

<sup>55</sup> Jesse, S., Kalinin, S. V., Proksch, R., Baddorf, A. P. & Rodriguez, B. J. The band excitation method in scanning probe microscopy for rapid mapping of energy dissipation on the nanoscale.

*Nanotechnology* **18**, 435503 (2007).

<sup>56</sup> Li, F., Zhang, S., Xu, Z., Wei, X. & Shrout, T. R. Critical Property in Relaxor-PbTiO<sub>3</sub> Single Crystals – Shear Piezoelectric Response. *Adv. Funct. Mater.* **21**, 2118-2128 (2011).

<sup>57</sup> Li, Y. W. & Li, F. X. Ultrahigh actuation strains in BaTiO<sub>3</sub> and Pb(Mn<sub>1/3</sub>Nb<sub>2/3</sub>)O<sub>3</sub>-PbTiO<sub>3</sub> single crystals via reversible electromechanical domain switching. *Appl. Phys. Lett.* **102**, 152905 (2013).

**Acknowledgements** Research supported by the National Science Foundation (NSF) through Penn State MRSEC grant DMR-0820404 (for T.T.A.L, Y.G, J.W., F.X, A.K., A.T.B, E.B., S.D. L.-Q.C. and V.G.) and grants DMR-1210588 (for A.N.M., L.-Q.C. and V.G.), DMR-0908718 (for A.N.M., L.-Q.C. and V.G.) and DMR-1006541(for L.-Q.C.). Phase-field simulations were carried out on the LION and Cyberstar clusters at Pennsylvania State University, partially supported by instrumentation funded through NSF grant OCI-0821527. The SXDM experiments in Fig. 3 were

conducted at the Center for Nanoscale Materials, a U.S. Department of Energy, Office of Science, Office of Basic Energy Sciences User Facility under Contract No. DE-AC02-06CD11357. The band-excitation piezoresponse force microscopy (BE-PFM) measurements in Fig. 4 were performed at the Center for Nanophase Materials Sciences, which is sponsored at Oak Ridge National Laboratory by the Scientific User Facilities Division, Office of Basic Energy Sciences, U.S. Department of Energy. The authors would like to thank S. R. Phillpot, S. Zhang, P. Wu, K. Lai and Y. Ren for useful discussions, and R.C. Haislmaier and M. B. Okatan for help with BE-PFM measurements and analysis.

**Author Contributions** The phase-field simulations were performed by Y.G., J.W., F. X. and L.-Q.C. The ferroelectric crystals were prepared by T.T.A.L., and characterized through SHG measurements by T.T.A.L., A.K., A.T.B., E.B., S.D. and V.G.; using Raman by T.T.A.L. and V.G.; by SXDM by T.T.A.L., M.H. and V.G.; by BE-PFM by T.T.A.L., S.L., A.K., A.B., and S.V.K. A.N.M., S.V.K.. T.T.A.L., S.L., A.B., A.N.M., and S.V.K. contributed to modelling of the PFM response. L.-Q.C. and V.G. guided the work. T.T.A.L. and V.G. wrote the manuscript. The work was initiated by L.-Q.C. and V.G. All authors discussed results and commented on the manuscript.

**Additional information** Supplementary Information is available in the online version of the paper. Reprints and permissions information is available online at [www.nature.com/reprints](http://www.nature.com/reprints). Correspondence and requests for materials should be addressed to V.G.

**Competing financial interests** The authors declare no competing financial interests.

## FIGURE LEGENDS

**Figure 1. Phase-field simulations showing how multi-domain structures can induce a thermotropic phase boundary in BaTiO<sub>3</sub>.** **a**, Volume fractions of orthorhombic (O, open blue triangles), tetragonal (T, open orange circles) and monoclinic (M<sub>C</sub>, open red diamonds) phases in an orthogonally twinned domain structure, upon quench-heating from 240 to 298 K. The phase classification in terms of discrete ferroelectric polarization ( $\mathbf{P}_s$ ) orientation ranges is shown in the legend in panel **c**. **b**, Stable volume phase fractions in the orthogonally twinned domain structure as a function of temperature. **c**, Selected area of the thermodynamically stabilized domain structure at 298 K. The legend indicates the color coding of the different ferroelectric phases, as well as their definition in terms of discrete polarization orientation ranges. Inset: zoom-in vector plot of a selected region showing local  $\mathbf{P}_s$  orientations.

**Figure 2. Local symmetry imaging and analysis by optical Second Harmonic Generation.** **a**, Scanning SHG microscopy image ( $I_X^{2\omega}$  with  $E_X^\omega$ ) of an in-plane *a,b*-domain structure in a BaTiO<sub>3</sub> single crystal *without* orthogonal twinning. The nonlinear optical tensor coefficients probed in the different domains for this experimental configuration are indicated, and corresponding ferroelectric polarization ( $\mathbf{P}_s$ ) axes are marked by double-headed white arrows. The scale bar corresponds to 8  $\mu\text{m}$ . **b**, Scanning SHG microscopy image ( $I_Y^{2\omega}$  with  $E_Y^\omega$ ) of an in-plane *a,b*-domain structure in a BaTiO<sub>3</sub> single crystal *with* orthogonal twinning. Also for this configuration, the polarization axes and active tensor coefficients are indicated. The scale bar corresponds to 12  $\mu\text{m}$ . **c**, SHG intensity polar plots of  $I_X^{2\omega}$  and  $I_Y^{2\omega}$  components (radius) versus fundamental polarization angle (azimuth angle  $\theta$ ) corresponding to the M<sub>C</sub> phase. Data points correspond to

experiment, and the solid lines correspond to theory based on a monoclinic  $m$  point group symmetry. **d**, Voigt notation form of both the second order nonlinear optical tensor and the piezoelectric tensor, which have the same symmetry attributes<sup>42</sup>. For tetragonal domains ( $4mm$  symmetry), only the tensor coefficients without superscript (in black) are nonzero, with  $d_{24} = d_{15}$  and  $d_{31} = d_{32}$ . For monoclinic  $m$  symmetry ( $m$  in-plane), the tensor coefficients with superscript  $m$  (in red) also become nonzero.

**Figure 3. Intrinsic shear distortion of the monoclinic Mc unit cell probed by nanoscale SXDM.** **a**, Extended 2D diffraction image of the (220) reflection ( $T^{220}$ ) from tetragonal  $b$ -domains in an orthogonally twinned BaTiO<sub>3</sub> crystal. The corresponding diffraction positions of coarse tetragonal  $a$ -domain twins ( $T_1^{202} = (\Delta 2\theta, \chi)_{T1} = (3.955, 9.163)$  and  $T_2^{202} = (\Delta 2\theta, \chi)_{T2} = (21.74, 9.163)$ ), or orthorhombic twins (see Supplementary Discussion 2.2) fall far outside the experimental zoom-in window used in our SXDM imaging (dashed white area). Panels **b** and **c** depict background-subtracted, normalized 2D (220) diffraction images corresponding to positions 2 and 3, respectively (see Fig. 3g). **d**, Reciprocal space map comparing diffraction peak positions ( $kl$ -plane projections around  $h = 2.000$ ) of experimentally observed tetragonal (T) and monoclinic (M) domains to those of hypothetical tetragonal (T1, T2) and orthorhombic (O3,O4) coarse twins. Solid lines  $\Delta K_i$  indicate the lever rules for the diffraction peak positions of potential nanotwinned adaptive phases. Axes are scaled by the reciprocal lattice unit ( $1.566 \text{ \AA}^{-1}$ ) of cubic (C) BaTiO<sub>3</sub> at 450 K<sup>28</sup>. The inset schematically depicts the Mc shear distortion (sheared  $m$  mirror plane shaded in red). **e**, Aspect-ratio corrected spatial map of the (220) Mc peak intensity in the orthogonally twinned BaTiO<sub>3</sub> structure. Scale bar: 10  $\mu\text{m}$ . **f**, Corresponding composite scanning SHG image ( $I_X^{2\omega} + a \cdot I_Y^{2\omega}$  with  $E_X^\omega$ , where  $a$  is scaled to match the SHG intensity in tetragonal domains).

Ferroelectric polarization ( $\mathbf{P}_s$ ) axes are marked by double-headed white arrows. Scale bar: 10  $\mu\text{m}$ .

**g**, Zoomed-in high-resolution spatial map (80 nm steps) of  $\Delta 2\theta = 2\theta^{220} - 2\theta^{T,\text{avg.}}$ ; the difference between the  $2\theta$  center of mass (COM) of the local (220) diffraction signal and the average  $2\theta$  COM of an undistorted tetragonal  $b$  domain. Scale bar: 10  $\mu\text{m}$ .

**Figure 4: Piezoelectric properties in the thermotropic phase boundary of BaTiO<sub>3</sub> at 298 K.**

**a**, Amplitude image of the vertical piezoresponse as measured by band-excitation Piezoresponse Force Microscopy (PFM)<sup>55</sup>. The cantilever arm in the measurement was oriented along X. Scale bar: 10  $\mu\text{m}$ . The inset shows a zoom-in on a selected area of the scan (2  $\mu\text{m}$  scale bar). **b**, Corresponding image of the phase of the vertical piezoresponse. Scale bar: 10  $\mu\text{m}$ . Where the piezoresponse was negligible, the phase was set to 0. **c**, Scanning SHG microscopy image ( $I_X^{2\omega}$  with  $E_X^\omega$ ) recorded in the same area. Here, the M<sub>C</sub> phase is marked by the regions of high SHG intensity. Scale bar: 10  $\mu\text{m}$ . **d**, Spatial maps of all phase-field calculated piezoelectric  $|d_{ij}|$  coefficients corresponding to the orthogonally twinned domain structure in Figure 1c (see Materials and Methods). The maps are arranged in Voigt tensor form to allow for direct comparison with Figure 2d.

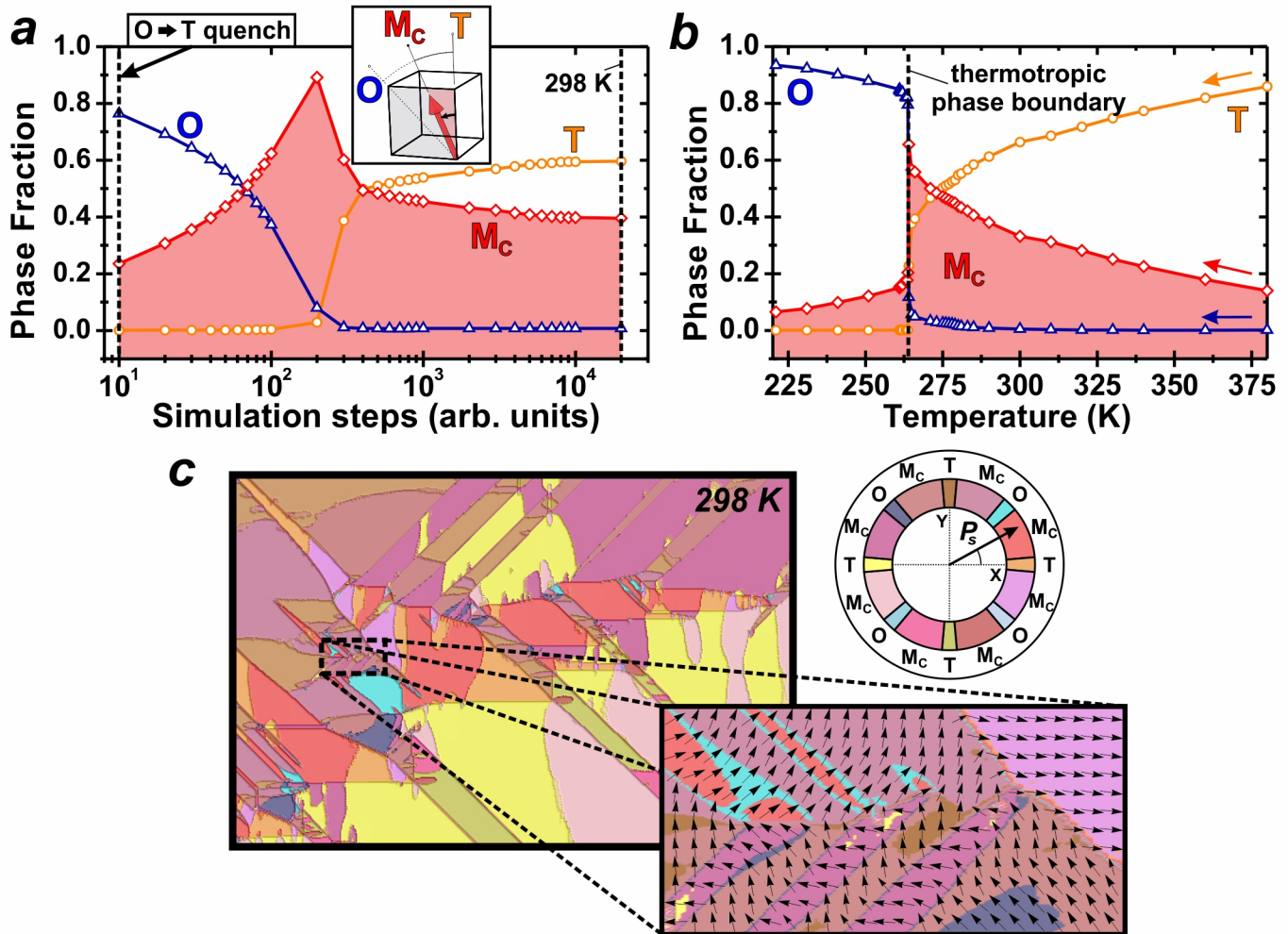


**Figure 1. Phase-field simulations showing how multi-domain structures can induce a thermotropic phase boundary in BaTiO<sub>3</sub>.** **a**, Volume fractions of orthorhombic (O, open blue triangles), tetragonal (T, open orange circles) and monoclinic (M<sub>C</sub>, open red diamonds) phases in an orthogonally twinned domain structure, upon quench-heating from 240 to 298 K. The phase classification in terms of discrete ferroelectric polarization ( $P_s$ ) orientation ranges is shown in the legend in panel **c**. **b**, Stable volume phase fractions in the orthogonally twinned domain structure as a function of temperature. **c**, Selected area of the thermodynamically stabilized domain structure at 298 K. The legend indicates the color coding of the different ferroelectric phases, as well as their definition in terms of discrete polarization orientation ranges. Inset: zoom-in vector plot of a selected region showing local  $P_s$  orientations.

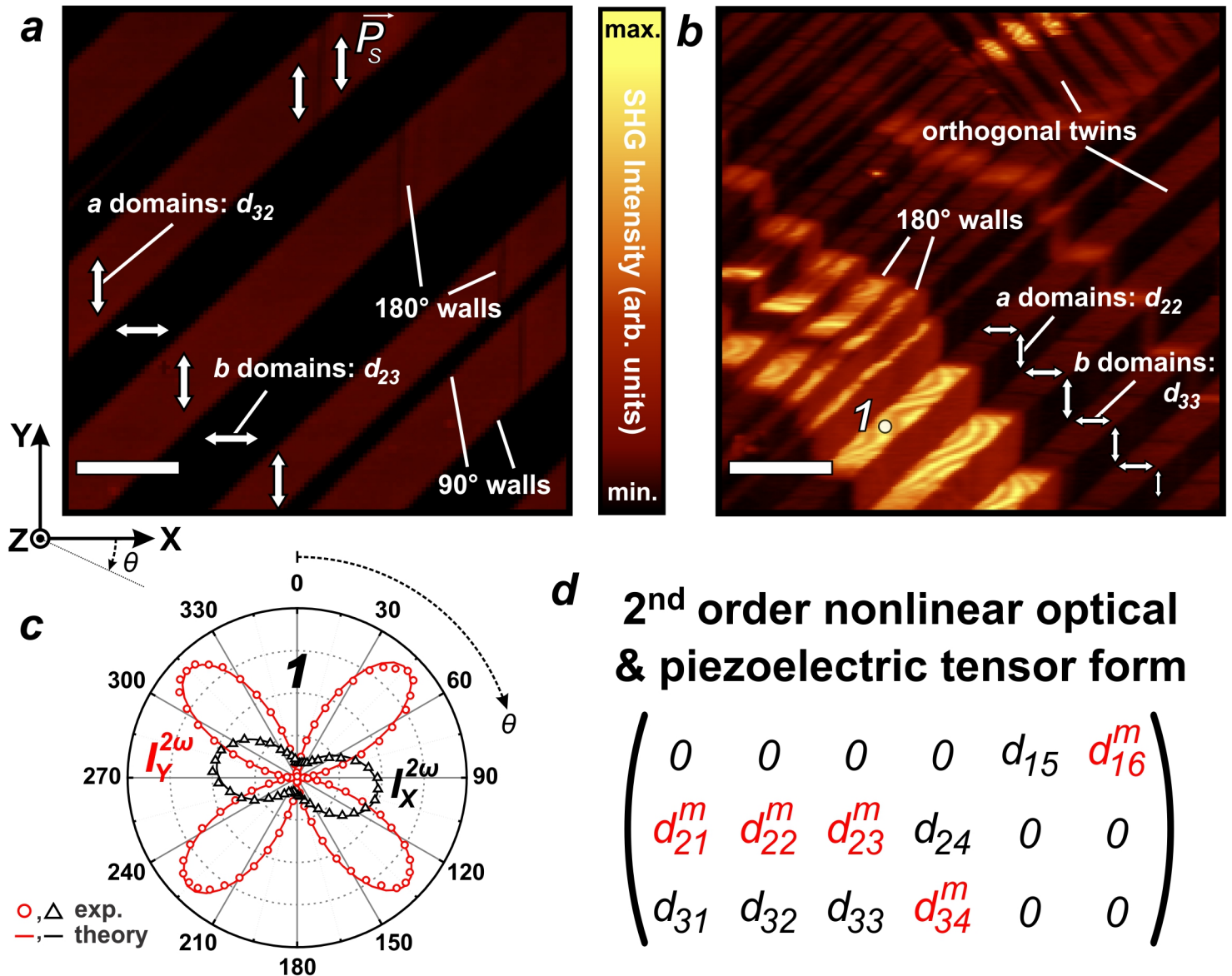


**Figure 2. Local symmetry imaging and analysis by optical Second Harmonic Generation.** **a**, Scanning SHG microscopy image ( $I_X^{2\omega}$  with  $E_X^\omega$ ) of an in-plane  $a,b$ -domain structure in a  $\text{BaTiO}_3$  single crystal *without* orthogonal twinning. The nonlinear optical tensor coefficients probed in the different domains for this experimental configuration are indicated, and corresponding ferroelectric polarization ( $P_s$ ) axes are marked by double-headed white arrows. Scale bar: 8  $\mu\text{m}$ . **b**, Scanning SHG microscopy image ( $I_Y^{2\omega}$  with  $E_Y^\omega$ ) of an in-plane  $a,b$ -domain structure in a  $\text{BaTiO}_3$  single crystal *with* orthogonal twinning. Also for this configuration, the polarization axes and active tensor coefficients are indicated. Scale bar: 12  $\mu\text{m}$ . **c**, SHG intensity polar plots of  $I_X^{2\omega}$  and  $I_Y^{2\omega}$  components (radius) versus fundamental polarization angle (azimuth angle  $\theta$ ) corresponding to the  $M_c$  phase. Data points correspond to experiment, and the solid lines correspond to theory based on a monoclinic  $m$  point group symmetry. **d**, Voigt notation form of both the second order nonlinear optical tensor and the piezoelectric tensor, which have the same symmetry attributes<sup>42</sup>. For tetragonal domains ( $4mm$  symmetry), only the tensor coefficients without superscript (in black) are nonzero, with  $d_{24}=d_{15}$  and  $d_{31}=d_{32}$ . For monoclinic  $m$  symmetry ( $m$  in-plane), the tensor coefficients with superscript  $m$  (in red) also become nonzero.

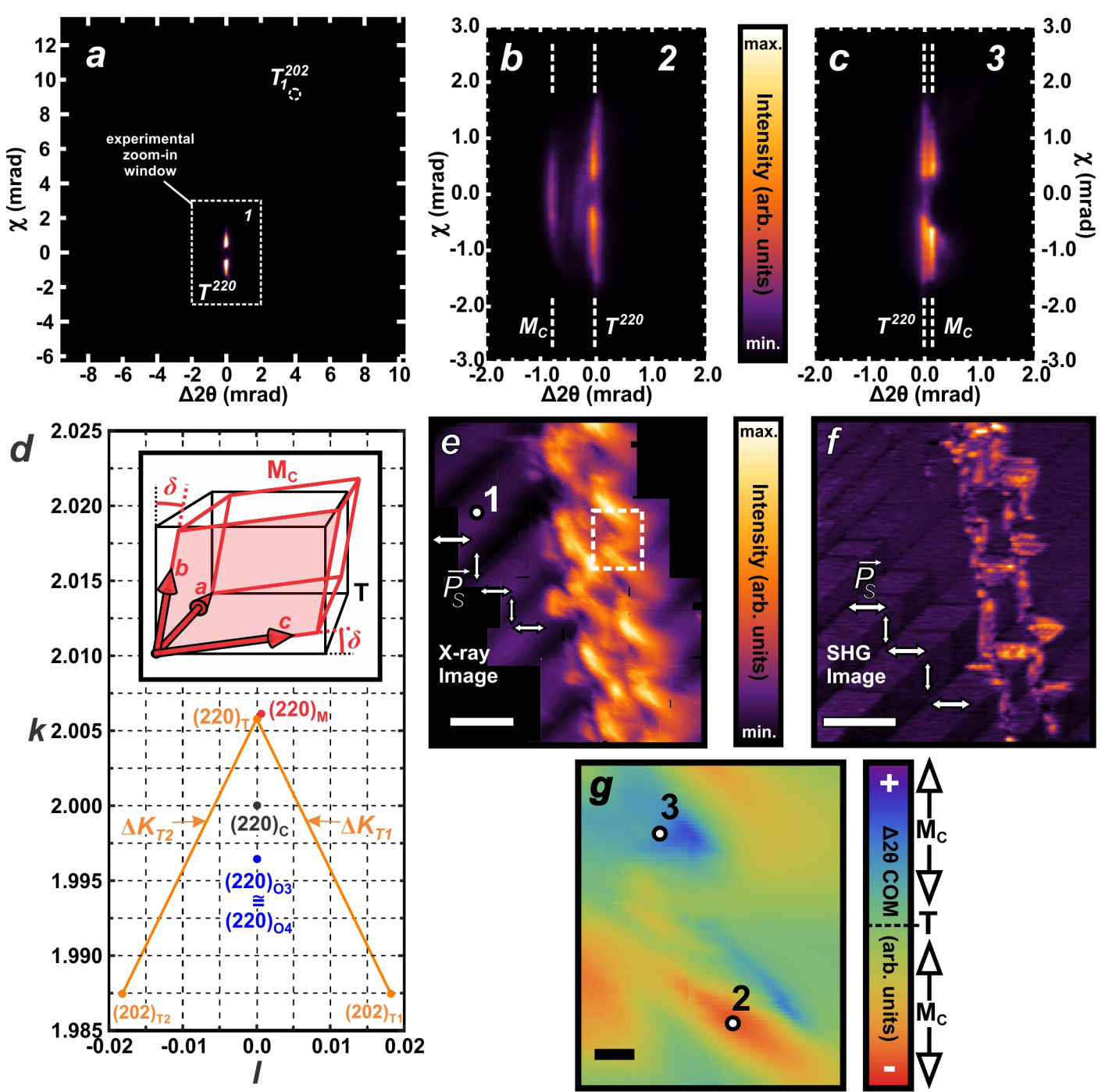


**Figure 3. Intrinsic shear distortion of the monoclinic  $M_c$  unit cell probed by nanoscale SXDM.** **a**, Extended 2D diffraction image of the (220) reflection ( $T^{220}$ ) from tetragonal  $b$ -domains in an orthogonally twinned  $\text{BaTiO}_3$  crystal. The corresponding diffraction positions of coarse tetragonal  $a$ -domain twins ( $T_1^{202} = (\Delta\theta, \chi)_{T_1} = (3.955, 9.163)$  and  $T_2^{202} = (\Delta\theta, \chi)_{T_2} = (21.74, 9.163)$ ), or orthorhombic twins (see Supplementary Discussion 2.2) fall far outside the experimental zoom-in window used in our SXDM imaging (dashed white area). Panels **b** and **c** depict background-subtracted, normalized 2D (220) diffraction images corresponding to positions 2 and 3, respectively (see Fig. 3g). **d**, Reciprocal space map comparing diffraction peak positions ( $kl$ -plane projections around  $h = 2.000$ ) of experimentally observed tetragonal (T) and monoclinic (M) domains to those of hypothetical tetragonal (T1, T2) and orthorhombic (O3,O4) coarse twins. Solid lines  $\Delta K_i$  indicate the lever rules for the diffraction peak positions of potential nanotwinned adaptive phases. Axes are scaled by the reciprocal lattice unit ( $1.566 \text{ \AA}^{-1}$ ) of cubic (C)  $\text{BaTiO}_3$  at  $450 \text{ K}$ <sup>28</sup>. The inset schematically depicts the  $M_c$  shear distortion (sheared  $m$  mirror plane shaded in red). **e**, Aspect-ratio corrected spatial map of the (220)  $M_c$  peak intensity in the orthogonally twinned  $\text{BaTiO}_3$  structure. Scale bar:  $10 \mu\text{m}$ . **f**, Corresponding composite scanning SHG image ( $I_X^{2\omega} + a \cdot I_Y^{2\omega}$  with  $E_Y^\omega$ , where  $a$  is scaled to match the SHG intensity in tetragonal domains. Ferroelectric polarization ( $P_s$ ) axes are marked by double-headed white arrows. Scale bar:  $10 \mu\text{m}$ . **g**, Zoomed-in high-resolution spatial map (80 nm steps) of  $\Delta\theta = 2\theta^{220} - 2\theta^{T,\text{avg}}$ ; the difference between the  $2\theta$  center of mass (COM) of the local (220) diffraction signal and the average  $2\theta$  COM of an undistorted tetragonal  $b$  domain. Scale bar:  $10 \mu\text{m}$ .

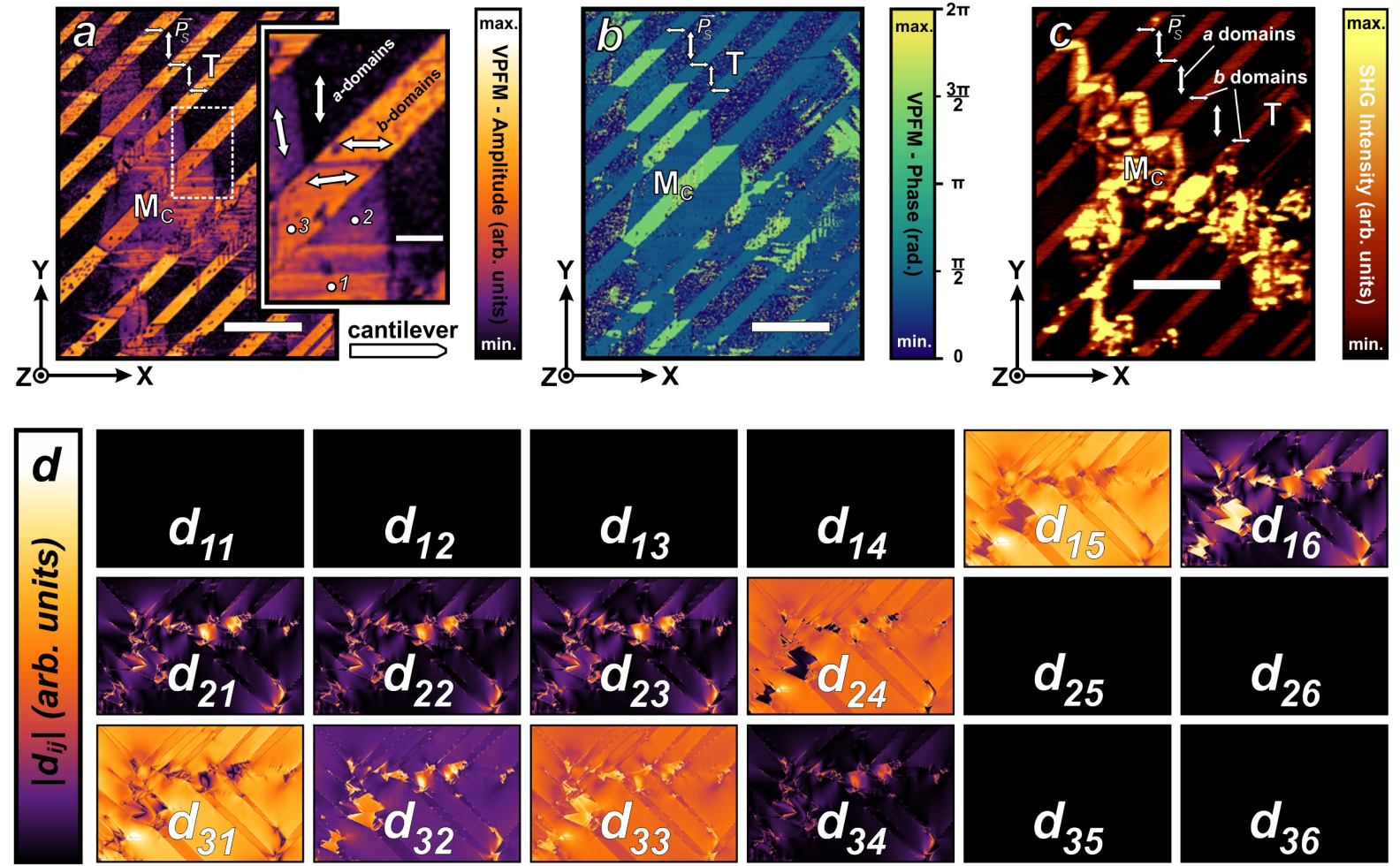


**Figure 4: Piezoelectric properties in the thermotropic phase boundary of  $\text{BaTiO}_3$  at 298 K. **a**, Amplitude image of the vertical piezoresponse as measured by band-excitation Piezoresponse Force Microscopy (PFM)<sup>55</sup>. The cantilever arm in the measurement was oriented along X. Scale bar: 10  $\mu\text{m}$ . The inset shows a zoom-in on a selected area of the scan (2  $\mu\text{m}$  scale bar). **b**, Corresponding image of the phase of the vertical piezoresponse. Scale bar: 10  $\mu\text{m}$ . Where the piezoresponse was negligible, the phase was set to 0. **c**, Scanning SHG microscopy image ( $I_X^{2\omega}$  with  $E_X^\omega$ ) recorded in the same area. Here, the  $M_C$  phase is marked by the regions of high SHG intensity. Scale bar: 10  $\mu\text{m}$ . **d**, Spatial maps of all phase-field calculated piezoelectric  $|d_{ij}|$  coefficients corresponding to the orthogonally twinned domain structure in Figure 1c (see Materials and Methods). The maps are arranged in Voigt tensor form to allow for direct comparison with Figure 2d.**

Supplementary Information for

## Thermotropic Phase Boundaries in Classic Ferroelectrics

Tom. T.A. Lummen<sup>1</sup>, Yijia Gu<sup>1</sup>, Jianjun Wang<sup>1,2</sup>, Shiming Lei<sup>1</sup>, Fei Xue<sup>1</sup>, Amit Kumar<sup>1,3</sup>, Andrew T. Barnes<sup>1</sup>, Eftihia Barnes<sup>1</sup>, Sava Denev<sup>1</sup>, Alex Belianinov<sup>3</sup>, Martin Holt<sup>4</sup>, Anna N. Morozovska<sup>5</sup>, Sergei V. Kalinin<sup>3</sup>, Long-Qing Chen<sup>1</sup> & Venkatraman Gopalan<sup>1,\*</sup>

<sup>1</sup>*Department of Materials Science and Engineering, Pennsylvania State University, University Park, Pennsylvania 16802, USA*

<sup>2</sup>*Department of Physics, University of Science and Technology Beijing, Beijing 100083, China*

<sup>3</sup>*Center for Nanophase Materials Sciences, Oak Ridge National Laboratory, Oak Ridge, Tennessee 37831, USA*

<sup>4</sup>*Center for Nanoscale Materials, Argonne National Laboratory, Argonne, IL 60439, USA*

<sup>5</sup>*Institute of Physics, National Academy of Sciences of Ukraine, 46, Nauki, 03028 Kiev, Ukraine*

\*To whom correspondence should be addressed; E-mail: [vxg8@psu.edu](mailto:vxg8@psu.edu)

### This PDF file includes:

- Materials and Methods
- Supplementary Discussions 1-4
- Supplementary Figures 1-13
- Supplementary References

## Materials and Methods

### Materials.

BaTiO<sub>3</sub> and KNbO<sub>3</sub> single crystals (typical size 5×5×1mm, {100}<sub>pc</sub> surface cut) were purchased from Fujian Castech Crystals Inc., China, and Oxide Corporation, Japan. Where necessary, additional polishing of crystal surfaces was performed to obtain satisfactory optical surface quality. Prior to experimental investigation, the samples were cooled through the (T→O) transition to about 240 K in a liquid nitrogen cooled cryostat, and kept there for 1 hour. Next, the samples were re-heated to ambient temperature (295 K), resulting in a typical multi-domain structure featuring interpenetrating, orthogonally twinned tetragonal *a* and *b* domains. Empirically, we determined that monoclinic signatures were readily found near such orthogonally twinned regions, which typically feature thin, wedge-shaped domains (e.g. see Supplementary Figure 1e). These M<sub>C</sub> signatures were reproducibly observed at room temperature after annealing the sample at 1150 K for 6 hours under a 50 cm<sup>3</sup>·min<sup>-1</sup> O<sub>2</sub> flow, excluding localized sample surface damage as the origin. This is consistent with the observation that Raman imaging using the 514 nm excitation wavelength at higher power densities tends to locally ‘erase’ the monoclinic signatures, which is presumably caused by the locally deposited thermal energy at this wavelength. The energy scale involved in this moderate ‘optical annealing’ process (local heating typically not exceeding the order of 50 K) is sufficient to rearrange the multi-domain structure, while being far below the energy required to induce reconstruction of a potentially damaged crystal surface (local temperatures on the order of 900 K). Furthermore, subsequent thermal cycling of the crystal after such optical erasure readily re-induces the monoclinic signatures. To allow for direct comparison, after thermal cycling the samples were kept at ambient temperature (295 K) in between and during SHG, Raman, nano-SXDM and BE-PFM experiments.

Phase field simulations.

Our three-dimensional (3D) phase-field model to describe the evolution of the spatial ferroelectric polarization distribution as a function of time is based on the time-dependent Ginzburg-Landau equation

$$\frac{\partial P_i(\mathbf{x},t)}{\partial t} = -L \frac{\delta F}{\delta P_i(\mathbf{x},t)}, \quad (i = X, Y, Z)$$

(eq. S1)

where  $\mathbf{P}$  is the ferroelectric polarization,  $\mathbf{x}$  is the spatial position in our XYZ Cartesian coordinate system and  $L$  is the kinetic relaxation coefficient related to the domain wall mobility. The total free energy  $F$  (a function of the polarization  $\mathbf{P}$ ) includes all the relevant energetic contributions  $f$ :

$$F = \int_V (f_{bulk} + f_{grad.} + f_{elas.} + f_{elec.}) dV,$$

(eq. S2)

i.e. the bulk, gradient, elastic and electrostatic contributions, respectively. The simulations were conducted for BaTiO<sub>3</sub> under stress-free boundary conditions. Stress ( $\sigma$ ) and strain ( $\varepsilon$ ) were calculated from the mechanical equilibrium condition<sup>58</sup>

$$\frac{\partial \sigma_{ij}}{\partial x_j} = 0, \quad (i = X, Y, Z; j = X, Y, Z)$$

(eq. S3)

where the  $\sigma_{ij}$  are the stress tensor components. The phenomenological potential and parameters (Landau-Devonshire coefficients, electrostrictive constant and elastic constant tensors) were taken from Li *et al.*<sup>59</sup>, and the modified isotropic gradient energy coefficients ( $g_{11}$ ,  $g_{12}$  and  $g_{44}$ ) were based on Hlinka *et al.*<sup>46</sup>. The electric field distribution in the multi-domain structure was calculated by first solving the Poisson equation to find the electric potential  $\varphi$ <sup>60</sup>, and then finding the electric field components through:

$$E_i = -\frac{\partial \varphi}{\partial x_i}, \quad (i = X, Y, Z)$$

(eq. S4)

The discretized quasi-two dimensional (quasi-2D) simulation size was  $1024\Delta x \times 1024\Delta x \times 4\Delta x$ , with a grid spacing of  $\Delta x = 1.8$  nm, unless otherwise specified. Periodic boundary conditions were imposed in all three directions. Due to the quasi-2D nature of the simulations, all domain structures and resulting properties were homogeneous along the out-of-plane  $z$ -direction. To obtain the orthogonally twinned initial multi-domain structure, we initially seeded two small sets of perpendicular tetragonal twins within the simulation system, filled the rest of the grid with thermal noise, and then allowed the system to relax at 380 K until stabilized. The phase diagram in Figure 1b was constructed by quenching this stabilized 380 K domain structure to a variety of lower temperatures in a set of parallel simulations, evolving the system in each of these until equilibration

was reached, and plotting the resulting volume phase fractions as a function of the equilibrium temperature.

*Second Harmonic Generation (SHG) microscopy and polarimetry.*

SHG microscopy and polarimetry were performed in reflection geometry using a modified Witec Alpha 300 S confocal Raman microscope equipped with a 10 nm-resolution *XYZ* piezo-translation stage. The in-plane  $\langle 100 \rangle$  crystallographic axes of the sample were carefully oriented along the *X* and *Y* axes of the experimental coordinate system. A pulsed fundamental beam (Spectra-Physics Tsunami (Ti:Sapphire),  $\omega = 800$  nm, 80 fs, 80 MHz, chopped at  $\approx 800$  Hz) was focused on the sample using a 100 $\times$  microscope objective (Nikon, N.A. 0.9) at a typical incident power density of about  $100 \text{ pJ} \cdot \mu\text{m}^{-2} \cdot \text{pulse}^{-1}$ . The lateral spatial resolution was close to diffraction-limited at  $\approx 355$  nm<sup>41</sup>. The polarization of the fundamental light was controlled by a zero-order half wave plate mounted in a motorized rotational stage. The second harmonic signal ( $2\omega$ ) was collected using the same objective, spectrally filtered and passed through a polarization analyzer prior to detection using a Hamamatsu R928 photo-multiplier tube. Nonlinear optical  $d_{ijk}$  coefficients were calculated using reference values for tetragonal BaTiO<sub>3</sub> taken from Miller's early work<sup>61,62</sup>, which were scaled using Miller's  $\Delta$  (which is assumed invariant for the SHG process in the same material<sup>63,64</sup>):

$$\Delta_{ijk} = \frac{d_{ijk}(-\omega_3; \omega_1, \omega_2)}{[n_i^2(\omega_3) - 1][n_j^2(\omega_1) - 1][n_k^2(\omega_2) - 1]}.$$

(eq. S5)

Here,  $\omega_3 = \omega_1 + \omega_2$  represents the SHG process, and the  $n_i(\omega)$  are the appropriate ordinary and extraordinary refractive indices of single domain BaTiO<sub>3</sub> at 295 K, as calculated using the known Sellmeier coefficients<sup>65</sup>. Induced nonlinear optical  $d_{ijk}$  coefficients were estimated by linear multiplication of these scaled  $d_{ijk}$  coefficients for tetragonal BaTiO<sub>3</sub> and the appropriate SHG intensity ratios (i.e.  $d_{ijk}$  ratios are taken the same as appropriate SHG intensity ratios obtained from the same scan). Note that both the nonlinear optical and piezoelectric tensors are third-rank polar tensors, and therefore subject to the same symmetry restrictions<sup>42</sup>. However, although they are also similarly labeled as  $d$ , they describe very different physical phenomena. All SHG experiments described in this work were performed in air, at ambient pressure and temperature (1 atm, 295 K). Monoclinic signatures were monitored as a function of time after thermal cycling and found to be stable up to at least 6 months when samples were kept at 295±2 K.

#### Raman microscopy.

Raman microscopy was performed in reflection geometry on the same modified Witec Alpha 300 S confocal Raman microscope. The in-plane ⟨100⟩ crystallographic axes of the sample were carefully oriented along the  $X$  and  $Y$  axes of the experimental coordinate system. The continuous wave 514.5 nm excitation beam (Melles Griot 43 Series Ar<sup>+</sup>-laser) was focused on the sample using a 100× microscope objective (Nikon, N.A. 0.9) at a typical incident power density of about 1 mW·μm<sup>-2</sup> (lateral spatial resolution ≈350 nm<sup>41</sup>). The polarization of the excitation light was controlled by a zero-order wave plate mounted in a rotational stage. The scattered Raman signal was collected using the same objective, spectrally filtered using an edge-pass filter (Semrock Inc.), and detected using an Acton Spectra-Pro 2300i monochromator equipped with a

thermoelectrically-cooled Andor DV401 CCD array. All Raman experiments described in this work were performed in air, at ambient pressure and temperature (1 atm, 295 K).

*Nanoscale Scanning X-ray Diffraction Microscopy (nano-SXDM).*

Nanoscale Scanning X-ray Diffraction Microscopy (nano-SXDM) experiments were performed using the Hard X-ray Nanoprobe (HXN) of the Center for Nanoscale Materials (CNM) at sector 26-ID-C of the Advanced Photon Source, Argonne National Laboratory. The coherent and monochromatic incident x-ray beam (photon energy 10.0 keV,  $\lambda = 1.2398 \text{ \AA}$ ) was focused on the sample by a Fresnel zone plate (Xradia Inc., 133  $\mu\text{m}$  diameter gold pattern, 24 nm outer zone, 300 nm thickness), yielding a  $\approx$ 30 nm full width half maximum lateral beam cross-section in the focal plane. To obtain such high spatial resolution, the center part of the radially symmetric focused beam was blocked by a 40  $\mu\text{m}$  diameter center stop attached to the zone plate, resulting in a lateral beam cross section in the form of an annulus of x-ray intensity<sup>44,45</sup>. The corresponding focused cone of x-rays had an incident angle spread of  $\approx$ 0.30°. The BaTiO<sub>3</sub> crystals ( $\{100\}$  surface) were rotationally oriented to the crystallographic Bragg diffraction condition of tetragonal *b* domains ((220) reflection), in a horizontal diffraction geometry. Diffraction peaks were recorded using a two-dimensional (2D) area CCD detector (Princeton PIXIS-XF: 1024F, 1024×1024 pixels, 13  $\mu\text{m}^2$  pixel size). Geometrical calibration parameters (sample-detector distance, detector centering and orientation) were determined from diffraction off a purely tetragonal domain using the focused beam. CCD images were recorded by 1.8 s of detector exposure, and background-corrected using a 1.8 s dark count image. Imaging of the sample was performed by stepwise lateral scanning of the x-ray zone plate relative to the sample using a hybrid optomechanical nanopositioning system, recording the diffraction image at each step. Simultaneous detection of element-specific x-ray

fluorescence allowed for positioning with respect to reference silver markers patterned on the sample surface. The focal plane was unambiguously established to within  $\approx 20\text{ }\mu\text{m}$  (the axial depth of focus) using the x-ray fluorescence signal of one of the patterned silver markers. To prevent *in-situ* domain structure rearrangement due to surface charging effects, a thin 5 nm layer of gold was deposited on the BaTiO<sub>3</sub> crystal surfaces and short-circuited to the sample mount. The addition of this thin conducting layer had no detectable effect on the observed domain structure, as confirmed by SHG imaging.

**Band-excitation Piezoresponse Force Microscopy (BE-PFM).**

Band-excitation Piezoresponse Force Microscopy (BE-PFM) experiments were performed on a Cypher AFM (Asylum Research) using Cr/Pt coated conductive tips (Multi-75E-G, Budget Sensors) at the Center for Nanophase Materials Sciences (CNMS) at Oak Ridge National Laboratory. Typical imaging scan sizes were  $30\times 30\text{ }\mu\text{m}$ , divided into a grid of  $256\times 256$  points. An AC driving voltage of 1.0 V was used. Details of the BE-PFM technique can be found elsewhere<sup>55</sup>. The resonance of the piezoelectric response measured at each grid point was fitted using a simple harmonic oscillator model and analyzed using a custom-written algorithm. Figure 4 plots corresponding images of fitted response parameters (PFM resonance amplitude and phase).

**FEM simulations of PFM response.**

The Finite Element Method (FEM) was utilized to model the piezoresponse in the PFM experiments<sup>66,67</sup>, using the commercial ANSYS™ software. In the present simulations, the tip was modelled as a truncated cone (tip height 10  $\mu\text{m}$ , full cone angle 30°) with a circular contact area (50 nm) with the sample surface<sup>67</sup>. The BaTiO<sub>3</sub> sample was modelled in an *X,Y,Z* reference frame

as a rectangular slab of  $8 \times 8 \times 1$   $\mu\text{m}$ . A decoupled approximation was assumed<sup>66-69</sup>; first the electric field distribution in the sample was calculated, which was then used as input in the subsequent calculation of the piezoresponse. For different polarization rotation values, the latter used appropriate dielectric and piezoelectric property tensors extracted from the multi-domain phase field simulations. The elastic properties of the monoclinic domain were assumed to be the same as that for tetragonal BaTiO<sub>3</sub><sup>70</sup>. A constant electric voltage of +1 V was applied to the tip surface, and the bottom surface of the sample slab was fixed to 0 V. In addition, the surface displacements ( $U_x$ ,  $U_y$ , and  $U_z$ ) were confined to 0 at the bottom of the sample (clamped bottom surface). The meshing was adjusted fine enough to yield results independent of the meshing size. Effective piezoelectric coefficients were estimated by linear multiplication of the FEM computed in-plane displacement in tetragonal  $b$  domains (using property tensors from multi-domain phase field simulations) by the appropriate ratios of VPFM amplitudes (i.e.  $U_i$ -ratios are taken the same as the corresponding VPFM amplitude ratios in the same scan).

#### Calculation of material properties from phase field simulations.

For the spatial property map calculations, the sets of local electric field ( $E_i^x$ ) and stress ( $\sigma_{ij}^x$ ) components at each spatial position  $x$  in the stabilized multi-domain structure (298 K, see Figure 1c) were extracted, with each set applied as external control parameters to a single BaTiO<sub>3</sub> domain in an independent single domain simulation. Extracted local electric field components were multiplied by a factor of 0.5 to ensure an equivalent electrostatic energy contribution in the single domain simulations (where the electric field is treated as external, rather than internal). This approach allowed for the evaluation of the intrinsic properties of the domains stabilized in the

multi-domain structure. Spatial maps of these local intrinsic properties were reconstructed using the grid site vectors  $\mathbf{x}$ .

Converse piezoelectric coefficients (in Voigt notation) were obtained from thermodynamic calculations using<sup>71</sup>:

$$d_{ij} = \sum_k \epsilon_0 \chi_{ik} g_{kj}, \quad (k = X, Y, Z; i = X, Y, Z; j = XX, YY, ZZ, YZ, XZ, XY) \quad (\text{eq. S6})$$

where  $\epsilon_0$  is the vacuum permittivity, and the piezoelectric coupling coefficient  $g_{ij}$  is calculated from the Gibbs free energy  $G$  as:

$$g_{ij} = -\frac{\partial^2 G}{\partial P_i \partial \sigma_j}. \quad (\text{eq. S7})$$

The dielectric susceptibility, defined as  $\chi_{ij} = \eta_{ij}^{-1}$ , is calculated through the dielectric stiffness:

$$\eta_{ij} = \epsilon_0 \frac{\partial^2 G}{\partial P_i \partial P_j}. \quad (\text{eq. S8})$$

Finally, all applied and calculated properties were transformed into the system of local symmetry coordinates (123), defined in analogy to the standard crystal physics axes adopted for tetragonal

$\text{BaTiO}_3$ <sup>42</sup>; at each grid site  $\mathbf{x}$ , the local 3 axis is assigned to the direction of the largest absolute  $XYZ$  component of the polarization  $\mathbf{P}_S$  (always in the  $XY$ -plane in our quasi-2D simulations), the local 1 axis is orthogonal to 3 and always along  $Z$ , and the local 2 axis is assigned to the in-plane direction orthogonal to 3, complementing the orthogonal right-handed coordinate system.

## Supplementary Discussion 1 - Origin of thermotropic behavior; internal domain stresses and fields

To clarify the origin of the observed thermotropic behavior and polarization rotation, we consider the internal electric field and stress components that are inherently present in an orthogonally twinned structure of competing ferroelectric domains. Supplementary Figure 1a shows a spatial map of the in-plane polarization rotation angle  $\beta$ , corresponding to the domain structure shown in Figure 1c. Here,  $\beta$  is defined as the absolute angular deviation of  $\mathbf{P}_S$  from the closest tetragonal  $\langle 001 \rangle$  direction, as calculated by the single domain simulations (see Methods). A strong spatial correlation is observed between  $\beta$  (Supplementary Figure 1a), the corresponding in-plane shear stress,  $\sigma_{23}$  (Supplementary Figure 1b), and the in-plane transverse electric field  $E_2$  (Supplementary Figure 1c) — i.e. the internal electric field component orthogonal to the nominal  $\langle 001 \rangle$  polarization axis.

These specific local stresses and electric fields arise from the internal mechanical constraints (through electrostriction) and polarization gradients (e.g. through domain wall bending) inherent to the network of orthogonally twinned domains. A large contribution to the internal electric fields arises from domain wall charging due to the slight bending of otherwise charge-neutral domain walls. As illustrated in Supplementary Figures 1d and e, a domain wall with a head-to-tail polarization geometry develops a bound charge density of  $\sigma_b = \mathbf{P}_S \bullet \hat{n} = P_\perp$ , where  $\hat{n}$  is the unit vector normal to the domain wall. Adding contributions from domains 1 and 2 on either side of a wall with bending angle  $\tau$  yields:

$$\sigma_b = P_\perp^1 + P_\perp^2 = -|P_S| \cos(\frac{\pi}{4} - \tau) + |P_S| \cos(\frac{\pi}{4} + \tau) = -\sqrt{2} |P_S| \sin \tau.$$

(eq. S9)

Thus, a finite wall bending angle  $\tau$  results in charging of the previously neutral domain wall, which in turn gives rise to an internal electric field.

## **Supplementary Discussion 2 – Exclusion of parent-phase nanotwinning**

In the following, we show that the monoclinic  $M_C$  phase in orthogonally twinned  $\text{BaTiO}_3$  corresponds to an *intrinsically* monoclinic structure. We show that an alternative interpretation of the observed  $M_C$  phase as an adaptive superlattice of nanoscale superlattice twins is unphysical and inconsistent with both theory and experiments on  $\text{BaTiO}_3$ . Considering the breadth of the issue, the discussion follows several steps:

- (1) We first briefly highlight the background, assumptions and key features of adaptive phase theory.
- (2) Next we use extended SXDM experiments covering a larger range of reciprocal space to exclude large domain twins of parent phase symmetry as the source of the observed  $M_C$  phase.
- (3) We then rule out any hypothetical nanotwinned superlattice by showing that for any potential adaptive phase, the observed  $M_C$  phase experimentally violates both the reciprocal space lever rule and the general invariance conditions dictated by adaptive phase theory.
- (4) Finally, we present high-resolution phase field results (grid spacing  $\Delta x = 0.5 \text{ nm}$ , on the order of the lattice constants) which show that even anomalously small domains on the 10 nm scale exhibit an *intrinsic* monoclinic symmetry. We further show that at room temperature where the  $M_C$  phase is observed, the relevant domain wall energy in bulk  $\text{BaTiO}_3$  is in fact finite and large, in direct contradiction with the essential assumption of adaptive phase theory.

### **1. Adaptive phase theory: background, assumptions and key features.**

In recent years, the microscopic structure of bridging ferroelectric phases observed in the MPBs of lead-based perovskite solid solutions has been thoroughly studied<sup>5</sup>. Where initial reports reported  $M_A$ ,  $M_B$  and/or  $M_C$  monoclinic structures in  $\text{Pb}(\text{Zr}_x\text{Ti}_{1-x})\text{O}_3$  (PZT)<sup>7,8,72</sup>, (1-

$x$ )Pb(Zn<sub>1/3</sub>Nb<sub>2/3</sub>)O<sub>3-x</sub>PbTiO<sub>3</sub> (PZN-PT)<sup>73-77</sup>, (1- $x$ )Pb(Mg<sub>1/3</sub>Nb<sub>2/3</sub>)O<sub>3-x</sub>PbTiO<sub>3</sub> (PMN-PT)<sup>75,78-80</sup> and (1- $x$ )Pb(Sc<sub>1/2</sub>Nb<sub>1/2</sub>)O<sub>3-x</sub>PbTiO<sub>3</sub> (PSN-PT)<sup>81,82</sup>, subsequent work showed that the observed diffraction signatures are also consistent with an adaptive ferroelectric phase consisting of a highly ordered conformal superlattice of nanoscale ferroelectric domain twins of parent phase symmetry, whose domain-averaged structure and symmetry is monoclinic<sup>30-33</sup>. Such nanoscale twinning can only occur when the ferroelectric domain wall energy goes to zero, *which is a pivotal assumption of adaptive phase theory*<sup>31,32,54</sup>. The observed lattice parameters of an adaptive phase correspond to a linear superposition of the lattice constants of the constituent nanotwins, weighted by the appropriate twin volume fractions. As a result, they exhibit a number of intrinsic crystallographic relationships<sup>31,33</sup>, while necessarily satisfying a set of general or special invariance conditions (the latter distinction depending on the presence of an applied electric field)<sup>31,32</sup>. The monoclinic structures observed in the MPBs of PMN-PT and PZN-PT were shown to adhere well to these relationships and conditions, which, combined with the experimental observation of domain twins down to a 10 nm scale in PMT-PT<sup>83,84</sup> and PZT<sup>34,85,86</sup>, argues for their adaptive nanostructured nature. Follow-up work by Wang *et al.*, established the diffraction theory of nanotwin superlattices, and quantified the adaptive diffraction phenomenon with a lever rule for the position of the adaptive diffraction peak in reciprocal space<sup>35-37</sup>, based on the same intrinsic crystallographic relationships. This lever rule dictates that a nanotwin superlattice peak,  $\mathbf{k}^s$ , necessarily lies in between the corresponding conventional diffraction peaks of the constituent twins in reciprocal space, on the straight line that connects them:

$$\mathbf{k}^s = \mathbf{K} + (1-\omega)\Delta\mathbf{K}, \quad (\text{eq. S10})$$

where  $\mathbf{K}$  is the relevant reciprocal space vector of the constituent crystal,  $\Delta\mathbf{K}$  is corresponding twin peak splitting vector, and  $\omega$  represents the twin variant volume fraction.

In summary, the key assumptions and features of adaptive phase theory are:

- i. a vanishing domain wall energy
- ii. crystallographic invariance conditions that intrinsically relate the adaptive phase lattice parameters to those of the constituent nanotwins
- iii. a corresponding lever rule for the adaptive diffraction peak position in reciprocal space

## **2. Excluding coarse ferroelectric twin domains using extended SXDM diffraction.**

First, we consider the fact that in the SXDM technique employed here, one uses a focused, highly monochromatic x-ray beam to selectively probe the microscopic structure only locally, as opposed to the ensemble-based conventional diffraction techniques which generally probe a far larger volume. Our experimental configuration is centered on the crystallographic (220) Bragg diffraction peak of tetragonal  $b$  domains, with the x-ray beam focused down to a  $\approx 30$  nm lateral cross section at an incident angle spread of  $\approx 0.30^\circ$ . Combined with the use of a 2D area CCD detector, we thus effectively probe a limited volume of reciprocal space around the corresponding (220) reciprocal space vector, with 30 nm spatial resolution (see Supplementary Figure 5). By rastering the beam across the sample and employing point-by-point sampling, we build up images of the local, nanoscale diffraction behavior.

Under the assumption that the observed  $M_C$  diffraction originates from an intrinsically monoclinic phase, our analysis below (Supplementary Discussion 3) shows the  $M_C$  phase to correspond to a distorted tetragonal structure, which has altered lattice constants ( $a_M = 3.9984 \text{ \AA}$ ;  $b_M = 3.9988 \text{ \AA}$ ;  $c_M = c_T = c = 4.0361 \text{ \AA}$ ) and which is sheared in the pseudocubic (100) plane that

is parallel to the sample surface ( $\delta_M = -0.018^\circ$ , see Supplementary Figure 12b). If one alternatively supposes the Mc phase to consist of a geometrically organized array of adaptive nanotwins, their structural superposition should emulate the observed monoclinic unit cell shear. There are only two possible pairs of parent phase nanotwins that could potentially achieve this: tetragonal twins with pseudocubic  $\{011\}$  twin planes (see Supplementary Figure 6a), or orthorhombic twins with pseudocubic  $\{010\}$  twin planes (Supplementary Figure 6b). With respect to the reference orientation of the  $b$ -domains, there are two possible orientations of a tetragonal  $a$ -domain twin (cases 1 and 2 in Supplementary Figure 6a), with corresponding relative in-plane rotation angles (around the sample surface normal) of  $\psi_1 = +0.523^\circ$  and  $\psi_2 = -0.523^\circ$ , respectively (where  $|\psi| = 90^\circ - 2 \tan^{-1}(a_T / c_T)$ ;  $a_T = 3.9994 \text{ \AA}$ ;  $c_T = 4.0361 \text{ \AA}$ ). We first consider how conventional diffraction from such twins (i.e. assuming coarse domains) relate to the (220) diffraction of tetragonal  $b$ -domains (labeled  $T^{220}$ ). A simple geometrical model shows that the corresponding (202) diffraction planes of these  $a$ -domain twins are rotated with respect to the (220) plane of the reference  $b$ -domains by ( $\Delta\alpha_1^{(202)} = -0.369^\circ$ ,  $\Delta\rho_1^{(202)} = 0.262^\circ$ ) and ( $\Delta\alpha_2^{(202)} = +0.369^\circ$ ,  $\Delta\rho_2^{(202)} = 0.262^\circ$ ), respectively, where  $\alpha$  and  $\rho$  are rotations around the  $Y$  and  $H$  axes indicated in Supplementary Figure 5b. This, combined with the larger  $d$ -spacing for the (202) planes ( $d^{(202)} = 1.4204 \text{ \AA}$ ), yields the following coordinates for their (202) diffraction in the experimental diffraction geometry: ( $T_1^{202} : 2\theta_1^{(202)} = 52.233^\circ$ ,  $\chi_1^{(202)} = 0.525^\circ$ ) and ( $T_2^{202} : 2\theta_2^{(202)} = 53.252^\circ$ ,  $\chi_2^{(202)} = 0.525^\circ$ ). As indicated in Figure 3a, which shows a representative large area CCD diffraction image of the  $b$ -domain  $T^{220}$  diffraction, the corresponding  $T_1^{202}$  diffraction peak falls far outside the experimental zoom-in window used in our SXDM imaging, whereas the  $T_2^{202}$  peak falls far outside even the large area detector range. In short, conventional diffraction from coarse  $a$ -

domain twins is clearly inconsistent with the observed  $M_C$  diffraction peak ( $2\theta_M = 52.017^\circ$ ,  $\chi_M = 0.005^\circ$ ). Similar geometrical arguments rule out conventional diffraction from the two orthorhombic twins sketched in Supplementary Figure 6b, (diffraction peaks  $O_3^{220}$  and  $O_4^{220}$ , respectively), as their lattice parameters yield relative  $\chi$ -coordinates far outside the experimental CCD range for (220) diffraction. For convenience and consistency, we use the pseudomonoclinic description of the orthorhombic structure in this discussion ( $a_o^M = 3.9874 \text{ \AA}$ ,  $b_o^M = c_o^M = 4.0812 \text{ \AA}$ ,  $\delta_o^M = 0.15^\circ$ )<sup>29</sup>. Thus, we can conclude that the  $M_C$  diffraction peaks observed in Figure 3 are not due to coarse twins of parent symmetry domains (i.e. domains twins larger than the coherence length of x-ray radiation; on the order of 1  $\mu\text{m}$  or above).

### **3. Ruling out hypothetical nanotwinned adaptive phases using extended SXDM diffraction.**

Knowing the relative structural orientations for the potential parent domain twins, we now consider the possibility of SXDM diffraction from an adaptive nanotwinned superlattice being responsible for the observed  $M_C$  peaks. As mentioned above, the lever rule (eq. S10) requires that the adaptive superlattice peak is positioned on the straight line between the conventional twin peaks in reciprocal space, with its exact position determined by the relative volume fractions of the constituent nanotwins. Moreover, due to their nanodomain-averaged nature, the corresponding observed lattice parameters of any adaptive phase necessarily satisfy a set of general invariance conditions. Below we will show that the observed  $M_C$  phase in fact violates both the lever rule and the general invariance conditions of any potential adaptive phase, ruling out a hypothetical nanotwinned substructure and confirming its *intrinsically* monoclinic nature.

Supplementary Figure 7 plots the relevant diffraction peaks of all parent domain twins considered above in reciprocal space, along with those of the cubic,  $M_C$ , and tetragonal  $b$ -domain

structures. The corresponding lattice parameters and relative geometric orientations are given in Supplementary Table 1 and Supplementary Figure 8, respectively. As is clear from these plots, the position of the  $M_C$  peak is inconsistent with any potentially applicable lever rule ( $\Delta\mathbf{K}_i$ , solid lines), in fact its shift is in an entirely different direction ( $\Delta\mathbf{q}_M = \mathbf{q}_M - \mathbf{q}_T = (0.0005, 0.0003, 0.0006)$ , see Supplementary Table 1), and as such the observed  $M_C$  phase cannot be explained through an adaptive phase description. This is also clearly seen by evaluating the invariance condition necessarily observed by adaptive phases<sup>31-33</sup>, which for tetragonal nanotwinning (Supplementary Figure 6a) dictates the relation of the adaptive lattice parameters ( $a_{ad.}$ ,  $b_{ad.}$ ,  $c_{ad.}$ ) to the corresponding tetragonal lattice parameters ( $a_t$ ,  $c_t$ ) as:  $a_{ad.} + c_{ad.} = a_t + c_t$  and  $b_{ad.} = a_t$ , where  $a_{ad.}$  and  $c_{ad.}$  are in the sheared plane. When applied to the lattice parameters of the  $M_C$  phase observed here ( $a_{ad.} = 3.9984 \text{ \AA}$ ,  $b_{ad.} = 3.9988 \text{ \AA}$ ,  $c_{ad.} = 4.0361 \text{ \AA}$ ), with tetragonal lattice parameters ( $a_t = 3.9994 \text{ \AA}$ ,  $b_t = 3.9994 \text{ \AA}$ ,  $c_t = 4.0361 \text{ \AA}$ ), there are two clear discrepancies: *i*) the condition  $b_{ad.} = a_t$  is not fulfilled, and *ii*)  $a_{ad.} < a_t$  dictates that  $c_{ad.} > c_t$ , which necessarily implies an unphysical twin variant volume fraction of  $\omega > 1$ , through the equation  $c_{ad.} = a_t + \omega(c_t - a_t)$ .

#### 4. *Domain size, and finite and large domain wall energy.*

To further assess the feasibility of a hypothetical adaptive nanotwin superlattice in BaTiO<sub>3</sub>, we next consider the required ferroelectric domain wall energy and corresponding domain size. A strict condition for the possible formation of an adaptive superlattice of nanoscale domain twins is a vanishing domain wall energy<sup>31,32,54</sup>. Although it has been argued that this effect occurs in the narrow compositional MPB regions of certain lead-based perovskite solid solutions, the domain wall energy is known to be finite in unpoled BaTiO<sub>3</sub> single crystals throughout the wide thermal stability range of the tetragonal phase<sup>46-47</sup> (280-380 K) in which the  $M_C$  phase is predicted to occur

(See Figure 1b). At 298 K, where we experimentally observe the  $M_C$  phase, the domain wall energy density for  $90^\circ$  head-to-tail walls is  $\approx 20 \text{ mJ m}^{-2}$  (Supplementary Figure 9). The finite and large domain wall energy in bulk BaTiO<sub>3</sub> is confirmed by experiments, in which tetragonal domain widths are nominally on a micron-scale<sup>16,17,21</sup>, as is also observed experimentally in this work. This indicates that *the crucial prerequisite for adaptive phase formation is simply not present here.*

The calculation of the domain wall energy is based on gradient coefficients that were self-consistently determined from inelastic neutron<sup>87</sup> and IR reflectivity<sup>88</sup> data by Hlinka and Marton<sup>46,47</sup>. They calculated the corresponding width of  $90^\circ$  head-to-tail domain walls in tetragonal BaTiO<sub>3</sub> to be  $\approx 3.6 \text{ nm}$  at ambient conditions, which is well supported by experiments<sup>48-53</sup>. As a consequence,  $90^\circ$  tetragonal domain twins cannot be smaller than  $\approx 7 \text{ nm}$ . Experimentally, even in very thin BaTiO<sub>3</sub> crystals the domain size behaves according to Kittel's law<sup>89,90</sup>, with the typical domain size width being  $\approx 25 \text{ nm}$  or more<sup>90</sup>. This is further confirmed by additional high-resolution phase-field simulations of an orthogonally domain-twinned BaTiO<sub>3</sub> system ( $4096\Delta x \times 4096\Delta x \times 4\Delta x$  grid with  $\Delta x = 0.5 \text{ nm}$ ); in which most domains are larger than 25 nm, and none are smaller than 7 nm (see Supplementary Figure 10). Moreover, as shown in Supplementary Figure 10e-g, even the smallest domains in the system exhibit a rotated ferroelectric polarization and monoclinic symmetry, underlining that the latter are intrinsic characteristics of the  $M_C$  phase even on the sub-30 nm length scale.

Summarizing, the observed  $M_C$  phase in BaTiO<sub>3</sub> is established as an *intrinsically* monoclinic phase. An alternative interpretation as an adaptive superlattice of nanoscale superlattice twins is shown to be unphysical and inconsistent with both theory and experiment.

## Supplementary Discussion 3 - Scanning X-ray Diffraction Microscopy

### 1. Scanning X-ray Diffraction Microscopy (SXDM) geometry.

The geometry of the nanoscale SXDM experiment is shown in Supplementary Figure 5a-b. The penetration depth ( $\approx 12 \mu\text{m}$ ) and angle of incidence ( $\approx 27.83^\circ$ ) of the incident x-ray beam in nano-SXDM yield an axially elongated probing volume at an angle to the sample surface, illuminating any domains in this volume and within  $\approx 5.6 \mu\text{m}$  of the sample surface (which is the x-ray attenuation length in BaTiO<sub>3</sub> (density  $6.02 \text{ g}\cdot\text{cm}^{-3}$ ) at 10.0 keV). Because of this angular depth-probing effect, T and Mc peaks can be observed simultaneously in individual diffraction images, and two dimensional maps (such as that in Figure 3f) appear more blurred than their normal incidence SHG counterparts, despite the greater lateral resolution of nano-SXDM.

### 2. Calculation of relative $2\theta$ center of mass (COM) in Fig. 3g.

The relative  $2\theta$  center of mass (COM) of the diffraction at each spatial position,  $\Delta 2\theta = 2\theta^{220} - 2\theta^{T,\text{avg.}}$ , was calculated in three steps: first, an  $I_{XRD}(2\theta)$ -‘spectrum’ was calculated by integration of the background-corrected (220) diffraction image along the  $\chi$ -axis; second, the  $2\theta$  COM of this spectrum was calculated via

$$2\theta^{220} = \frac{\sum_i 2\theta_i \cdot I_{XRD,i}}{\sum_i I_{XRD,i}}, \quad (\text{eq. S11})$$

and third, the averaged  $2\theta$  COM value of the diffraction signal from only the T-peak recorded in a purely tetragonal reference domain,  $2\theta^{T,\text{avg.}}$ , was subtracted. CCD diffraction images and

$I_{XRD}(2\theta)$  data were normalized to the maximum integrated intensity in the corresponding scan series. As illustrated in Supplementary Figure 11c, the relative  $2\theta$  center of mass (COM)  $M_C$  diffraction peak is found to vary on a length scale on the order of  $\approx 1 \mu\text{m}$ , while the position of the tetragonal T peak remains largely unchanged (see also Figure 3g). The absence of nanoscale structural variation shows that there are no nano-domains down to a 30 nm scale.

### 3. SXDM rocking curve analysis.

Supplementary Figure 11 shows the variation of both the (220) T and  $M_C$  peaks from a single spatial position in a selected  $b$ -domain as a function of the sample angle  $\omega$  (equivalent to a traditional rocking curve). As illustrated by the series of (220) diffraction images, the  $M_C$  peak consistently diffracts to a higher  $2\theta$  than the T peak throughout this rocking curve. Moreover, upon increasing  $\omega$ , the  $M_C$  peak both appears and disappears at lower sample angles compared to the T peak. These two observations combined show that the difference between the diffracting  $M_C$  and T planes is mainly due to a rotation of the diffraction planes around axis  $Y$ , as indicated by angle  $\alpha$  in Supplementary Figure 5b. By contrast, a pure change in lattice plane spacing ( $d$ -spacing) would have resulted in either the  $M_C$  peak being at a lower  $2\theta$  than the T-peak (larger  $d$ ), or the  $M_C$  peak disappearing at a larger  $\omega$  than the T peak (smaller  $d$ ). The center diffraction condition of the peaks is defined by the sample angle  $\omega$  at which the on-axis portion of the incident beam is diffracted by the corresponding set of diffraction planes. The variation of the integrated intensity of each diffraction peak with the sample angle  $\omega$  yields a symmetric double-maximum curve due to the annular beam cross-section (Supplementary Figure 11b), and the center of mass of this curve defines the center diffraction condition for that peak. This yields  $\omega_T = 27.834^\circ$  and  $\omega_M = 27.822^\circ$  for the T and  $M_C$  peaks, respectively, and an extracted plane rotation of

$\alpha \equiv \omega_M - \omega_T = -0.012^\circ$ . The peak positions (at their center diffraction condition) are ( $2\theta_T = 52.006^\circ, \chi_T \equiv 0$ ) and ( $2\theta_M = 52.017^\circ, \chi_M = 0.005^\circ$ ), respectively, corresponding to  $d$ -spacings of  $d_T = 1.4140 \text{ \AA}$  and  $d_M = 1.4137 \text{ \AA}$  for the respective (220) reflections. The  $d_T$  value corresponds to a tetragonal lattice constant of  $a_T = 3.9994 \text{ \AA}$ , consistent with values found in literature<sup>25,26,28,29,91</sup>.

#### 4. Geometrical shear model

With the Mc phase anticipated to be an intermediate bridging phase between the tetragonal and orthorhombic structures, we consider a simple shear distortion of the tetragonal unit cell as a geometrical model (Supplementary Figure 12a). Because we found rotation of the diffraction plane to be the dominant distortion contribution, we initially assume the edge lengths of the sheared Mc parallelepiped to remain equal to the tetragonal lattice constants  $a_T = 3.9994 \text{ \AA}$  and  $c_T = 4.0361 \text{ \AA}$  ( $c_T$  was taken from Ref. 91). Then, based on the experimentally determined relative (220) plane rotation of  $\alpha = -0.012^\circ$ , we use the simple geometrical model to estimate a corresponding shear angle  $\delta_M$  of  $-0.018^\circ$  (see Supplementary Figure 12a). When compared to anticipated values for the tetragonal and orthorhombic unit cells ( $\delta_T = 0^\circ$  and  $\delta_O = -0.075^\circ$ , the latter in its pseudomonoclinic description<sup>29</sup>), this value clearly establishes the Mc-phase as an intermediate between the T and O phases. Both the change in  $d$ -spacing and the relative tilting (rotation around axis H by angle  $\rho$ ) of the Mc diffraction planes are negligible in the pure shear model at this  $\delta_M$ . The experimentally observed  $d$ -spacing decrease ( $\Delta d \equiv d_M - d_T = -0.0003 \text{ \AA}$ ) and out-of-plane tilting ( $\Delta\chi \equiv \chi_M - \chi_T = 0.005^\circ$ ) are likely the result of small changes in lattice constants that accompany the unit cell shearing (i.e. changes in the edge lengths of the sheared Mc parallelepiped).

Based on the experimental  $\Delta d$  and  $\Delta\chi$  values (both are dependent on  $a_M$  and  $b_M$ , see Supplementary Figure 12b), a simple geometrical calculation for the sheared (220) diffraction plane with  $\delta_M = -0.018^\circ$  yields corresponding values of  $a_M = 3.9984 \text{ \AA}$  and  $b_M = 3.9988 \text{ \AA}$ . The fact that the tetragonal  $a$  axis, perpendicular to the sheared plane, shortens more than  $b$  is consistent with an intermediate cell; on full transformation to the orthorhombic phase, the  $a$  axis is expected to shorten, while the  $b$  axis is expected to elongate, both by significantly larger amounts<sup>23</sup>. Recalculation of the shear angle  $\delta_M$  using the new  $a_M$  and  $b_M$  constants yields the same value (-0.018°), confirming the validity of our initial assumption of constant edge-lengths. Finally, we note that the exact value of  $c$  has no significant effect on the shear angle assessment (we took  $c_M = c_T = c = 4.0361 \text{ \AA}$  for all calculations).

## Supplementary Discussion 4 - FEM simulations of piezoresponse

We used FEM simulations to calculate the sample surface displacements  $U_x$ ,  $U_y$  and  $U_z$  in a single monoclinic BaTiO<sub>3</sub> domain in contact with a PFM tip, using the corresponding dielectric and piezoelectric properties calculated from phase-field simulations (See Materials and Methods). In the FEM simulations, the rotation angle of the ferroelectric polarization in the monoclinic domain,  $\beta$ , is defined with respect to the X direction (i.e. polarization rotation occurs in the XY-plane). Due to the in-plane orientation of the domains ( $P_s \perp Z$ ), the out-of-plane displacement of the sample surface,  $U_z$ , is negligible as compared to  $U_x$  and  $U_y$ . Consequently, the vertical PFM (VPFM) response shown in Figures 4a and b is due to buckling of the cantilever arm, induced by *in-plane* displacements of the sample surface parallel to the cantilever arm. Given the experimental cantilever geometry, the VPFM response in *b*- and *a*-domains is governed by the simulated  $U_x$  and  $U_y$  displacements, respectively. We use the in-plane displacement obtained for tetragonal *b*-domains from the FEM simulations —  $U_x^{\beta=0^\circ} = -146$  pm at +1.0 V — to calibrate the experimental piezoresponse. As seen in the inset of Figure 4a, in the M<sub>C</sub> phase the *b*-domains exhibit a slightly reduced displacement (corresponding to  $U_x \approx 114$  pm V<sup>-1</sup>, position 3), while the monoclinic *a*-domains show newly induced displacements that are entirely absent in the tetragonal phase ( $U_y \approx 43$  pm V<sup>-1</sup> and 105 pm V<sup>-1</sup> in positions 2 and 1, respectively). Supplementary Figure 13a plots the relative contributions of the individual  $d_{ij}$  piezoelectric coefficients to  $U_x$ , showing its main contributions arise from  $d_{15}$ ,  $d_{24}$  and  $d_{33}$ . As shown in Supplementary Figure 13b, it is the suppression of  $d_{15}$  that dominates the reduction of  $U_x$  with increasing polarization rotation  $\beta$ . Supplementary Figure 13c plots the relative contributions of the individual  $d_{ij}$  piezoelectric

coefficients to  $U_y$ , showing its main contributions are from  $d_{22}$  and  $d_{16}$ . Here the induced nonzero value of  $U_y$  is the combined effect of both these coefficients, which become nonzero as  $\beta$  increases (Supplementary Figure 13d). Given the FEM-calibrated experimental in-plane displacements, we estimate the polarization rotation angles at positions 1, 2 and 3 in Figure 4a to be 15, 7 and 17°, respectively.

## Supplementary References

- <sup>58</sup> Khachaturyan, A. G. *Theory of Structural Transformations in Solids*. Dover Publications Inc., Mineola, New York, 2008. ISBN 0486462803.
- <sup>59</sup> Li, Y. L., Cross, L. E., & Chen, L.-Q. A phenomenological thermodynamic potential for BaTiO<sub>3</sub> single crystals. *J. Appl. Phys.* **98**, 064101 (2005).
- <sup>60</sup> Li, Y. L., Hu, S. Y., Liu, Z. K. & Chen, L.-Q. Effect of electrical boundary conditions on ferroelectric domain structures in thin films. *Appl. Phys. Lett.* **81**, 427 (2002).
- <sup>61</sup> Miller, R. C., Kleinman, D. A. & Savage, A. Quantitative studies of optical harmonic generation in CdS, BaTiO<sub>3</sub>, and KH<sub>2</sub>PO<sub>4</sub> type crystals. *Phys. Rev. Lett.* **11**, 146 (1963).
- <sup>62</sup> Miller R. C. Optical Harmonic Generation in Single Crystal BaTiO<sub>3</sub>. *Phys. Rev.* **134**, A1313 (1964).
- <sup>63</sup> Miller, R. C. Optical second harmonic generation in piezoelectric crystals. *Appl. Phys. Lett.* **5**, 17 (1964).
- <sup>64</sup> Shoji, I., Kondo, T., Kitamoto, A., Shirane, M. & Ito, R. Absolute scale of second-order nonlinear-optical coefficients. *J. Opt. Soc. Am. B* **14**, 2268 (1997).
- <sup>65</sup> K. Buse, *et al.* Refractive Indices of Single Domain BaTiO<sub>3</sub> for Different Wavelengths and Temperatures. *Phys. Stat. Sol. A* **135**, K87 (1993).

<sup>66</sup> Scrymgeour, D.A. & Gopalan V. Nanoscale piezoelectric response across a single antiparallel ferroelectric domain wall. *Phys. Rev. B* **72**, 024103 (2005).

<sup>67</sup> Lei S., *et al.* Origin of piezoelectric response under a biased scanning probe microscopy tip across a 180° ferroelectric domain wall. *Phys. Rev. B* **86**, 134115 (2012).

<sup>68</sup> Felten, F., Schneider, G.A., Saldana. J.M. & Kalinin S. V. Modeling and measurement of surface displacements in BaTiO<sub>3</sub> bulk material in piezoresponse force microscopy. *J. Appl. Phys.* **96**, 563-568 (2004).

<sup>69</sup> Morozovska, A.N., Eliseev, E. A., Bravina, S. L. & Kalinin S. V. Resolution-function theory in piezoresponse force microscopy: Wall imaging, spectroscopy, and lateral resolution. *Phys. Rev. B* **75**, 174109 (2007).

<sup>70</sup> Zgonik, M. *et al.* Dielectric, elastic, piezoelectric, electro-optic, and elastic-optic tensors of BaTiO<sub>3</sub>. *Phys. Rev. B* **50**, 5941 (1994).

<sup>71</sup> Haun, M. J., Furman, E., Jang, S.J. & Cross, L. E. Thermodynamic Theory of the Lead Zirconate-Titanate Solid Solution System, Part V: Theoretical Calculations. *Ferroelectrics* **99**, 63 (1989).

<sup>72</sup> Noheda, B. *et al.* A monoclinic ferroelectric phase in the Pb(Zr<sub>1-x</sub>Ti<sub>x</sub>)O<sub>3</sub> solid solution. *Appl. Phys. Lett.* **74**, 2059–2061 (1999).

<sup>73</sup> Noheda, B. *et al.* Polarization Rotation via a Monoclinic Phase in the Piezoelectric 92%PbZn<sub>1/3</sub>Nb<sub>2/3</sub>O<sub>3</sub>-8%PbTiO<sub>3</sub>. *Phys. Rev. Lett.* **86**, 3891-3894 (2001).

<sup>74</sup> La-Orautapong, D. *et al.* Phase diagram of the relaxor ferroelectric (1-x)PbZn<sub>1/3</sub>Nb<sub>2/3</sub>O<sub>3</sub>-xPbTiO<sub>3</sub>. *Phys. Rev. B* **65**, 144101 (2002).

<sup>75</sup> Kiat, J.-M. *et al.* Monoclinic structure of unpoled morphotropic high piezoelectric PMT-PT and PZN-PT compounds. *Phys. Rev. B* **65**, 064106 (2002).

- <sup>76</sup> Noheda, B. *et al.* Electric-field-induced phase transitions in rhombohedral  $\text{Pb}(\text{Zn}_{1/3}\text{Nb}_{2/3})_{1-x}\text{Ti}_x\text{O}_3$ . *Phys. Rev. B* **65**, 244101 (2002).
- <sup>77</sup> Ohwada, K. *et al.* Neutron diffraction study of field-cooling effects on the relaxor ferroelectric  $\text{Pb}[(\text{Zn}_{1/3}\text{Nb}_{2/3})_{0.92}\text{Ti}_{0.08}]\text{O}_3$ . *Phys. Rev. B* **67**, 094111 (2003).
- <sup>78</sup> Singh, A. K. *et al.* Structure and the location of the morphotropic phase boundary region in  $(1-x)[\text{Pb}(\text{Mg}_{1/3}\text{Nb}_{2/3})\text{O}_3]-x\text{PbTiO}_3$ . *J. Phys.: Condens. Matter* **13**, L931-L936 (2001).
- <sup>79</sup> Noheda, B. *et al.* Phase diagram of the ferroelectric relaxor  $(1-x)\text{PbMg}_{1/3}\text{Nb}_{2/3}\text{O}_3-x\text{PbTiO}_3$ . *Phys. Rev. B* **66**, 054104 (2002).
- <sup>80</sup> Bai, F. *et al.* X-ray and neutron diffraction investigations of the structural phase transformation sequence under electric field in  $0.7\text{Pb}(\text{Mg}_{1/3}\text{Nb}_{2/3})\text{O}_3-0.3\text{PbTiO}_3$  crystal. *J. Appl. Phys.* **96**, 1620-1627 (2004).
- <sup>81</sup> Haumont, R. *et al.* Cationic-competition-induced monoclinic phase in high piezoelectric  $(\text{PbSc}_{1/2}\text{Nb}_{1/2}\text{O}_3)_{1-x}-(\text{PbTiO}_3)_x$ . *Phys. Rev. B* **68**, 014114 (2003).
- <sup>82</sup> Haumont, R. *et al.* Morphotropic phase boundary of heterovalent perovskite solid solutions: Experimental and theoretical investigation of  $\text{PbSc}_{1/2}\text{Nb}_{1/2}\text{O}_3-\text{PbTiO}_3$ . *Phys. Rev. B* **71**, 104106 (2005).
- <sup>83</sup> Wang, H. *et al.* Hierarchical micro-/nanoscale domain structure in  $\text{Mc}$  phase of  $(1-x)\text{Pb}(\text{Mg}_{1/3}\text{Nb}_{2/3})\text{O}_3-x\text{PbTiO}_3$  single crystal. *Appl. Phys. Lett.* **89**, 042908 (2006).
- <sup>84</sup> Wang, H. *et al.* Hierarchical Domain Structure of Adaptive  $\text{M}_\text{B}$  phase in  $\text{Pb}(\text{Mg}_{1/3}\text{Nb}_{2/3})\text{O}_3-32\%\text{PbTiO}_3$  Single Crystal. *J. Am. Ceram. Soc.* **91**, 2382-2384 (2008).
- <sup>85</sup> Schmitt, L. A. *et al.* Composition dependence of the domain configuration and size in  $\text{Pb}(\text{Zr}_{1-x}\text{Ti}_x)\text{O}_3$  ceramics. *J. Appl. Phys.* **101**, 074107 (2007).
- <sup>86</sup> Theissmann, R. *et al.* Nanodomains in morphotropic lead zirconate titanate ceramics: On the

origin of the strong piezoelectric effect. *J. Appl. Phys.* **102**, 024111 (2007).

<sup>87</sup> Harada, J., Axe, J. D. & Shirane, G. Neutron-Scattering Study of Soft Modes in Cubic BaTiO<sub>3</sub>. *Phys. Rev. B* **4**, 155-163 (1971).

<sup>88</sup> Hlinka, J., et al. Infrared dielectric response of relaxor ferroelectrics. *Phase Transitions* **79**, 41-78 (2006).

<sup>89</sup> Kittel, C. Physical Theory of Ferromagnetic Domains. *Rev. Mod. Phys.* **21**, 541 (1949).

<sup>90</sup> Shilling, A. et al. Scaling of domain periodicity with thickness measured in BaTiO<sub>3</sub> single crystal lamellae and comparison with other ferroics. *Phys. Rev. B* **74**, 024115 (2006).

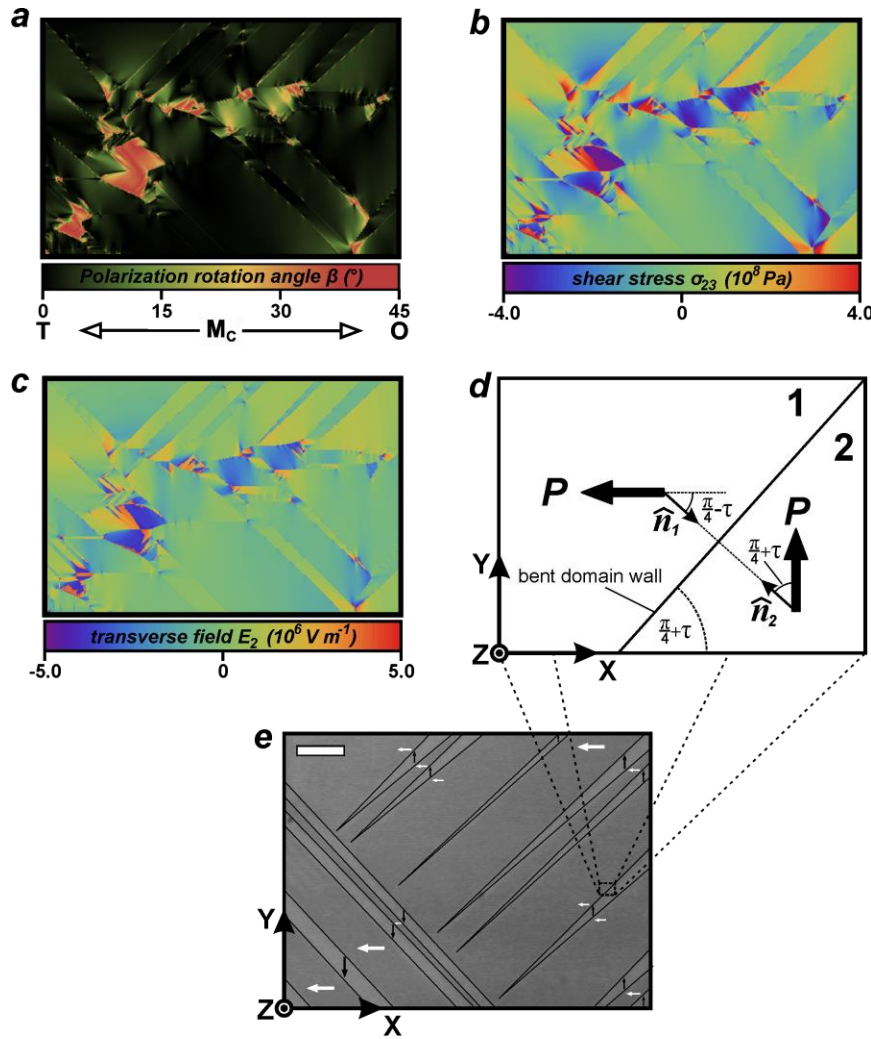
<sup>91</sup> Holt, M., Hassani, K. & Sutton, M. Microstructure of Ferroelectric Domains in BaTiO<sub>3</sub> Observed via X-Ray Microdiffraction. *Phys. Rev. Lett.* **95**, 085504 (2005).

<sup>92</sup> Loudon, R. The Raman effect in crystals. *Adv. Phys.* **50**, 813 (2001).

<sup>93</sup> El Marssi, M., Marrec, F. L., Lukyanchuk, I. A. & Karkut, M.G. Ferroelectric transition in an epitaxial barium titanate thin film: Raman spectroscopy and x-ray diffraction study. *J. Appl. Phys.* **94**, 3307 (2003). And references therein.

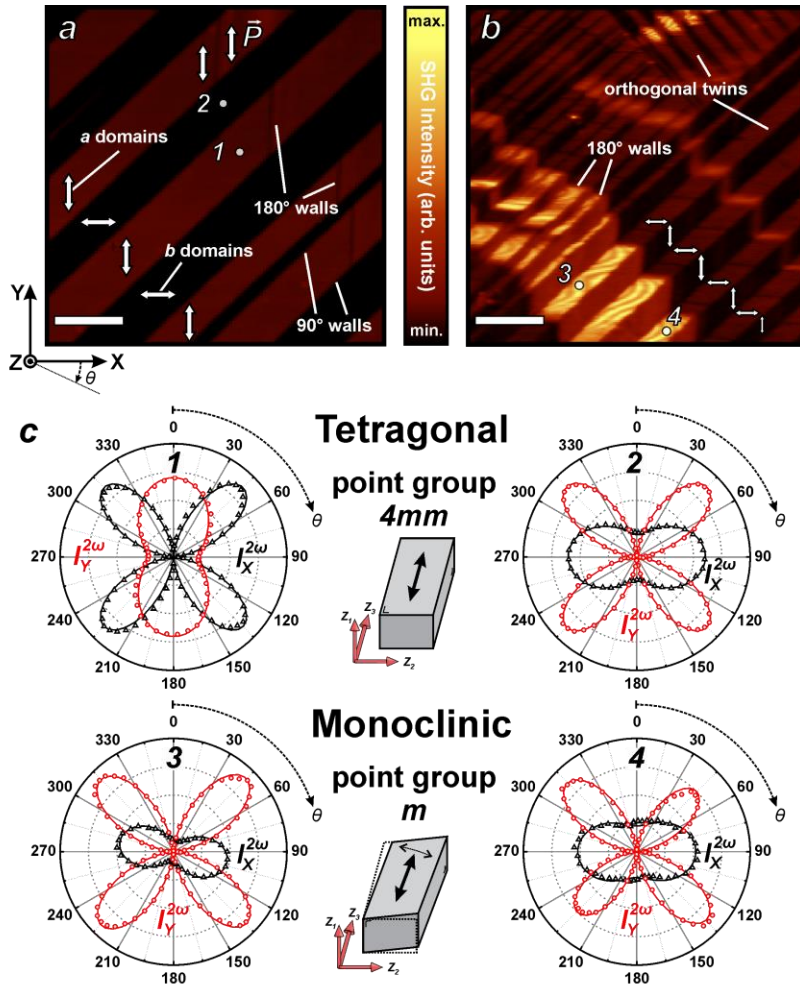
<sup>94</sup> Robins, L. H. et al. Investigation of the structure of barium titanate thin films by Raman spectroscopy. *J. Appl. Phys.* **76**, 7487 (1994). And references therein.

<sup>95</sup> Anokhin, A. S., Yuzyuk, Y. I., Golovko, Y. I., Mukhortov, V.M. & El Marssi, M. Electric-field-induced monoclinic phase in (Ba,Sr)TiO<sub>3</sub> thin film. *J. Appl. Phys.* **109**, 074111 (2011). And references therein.



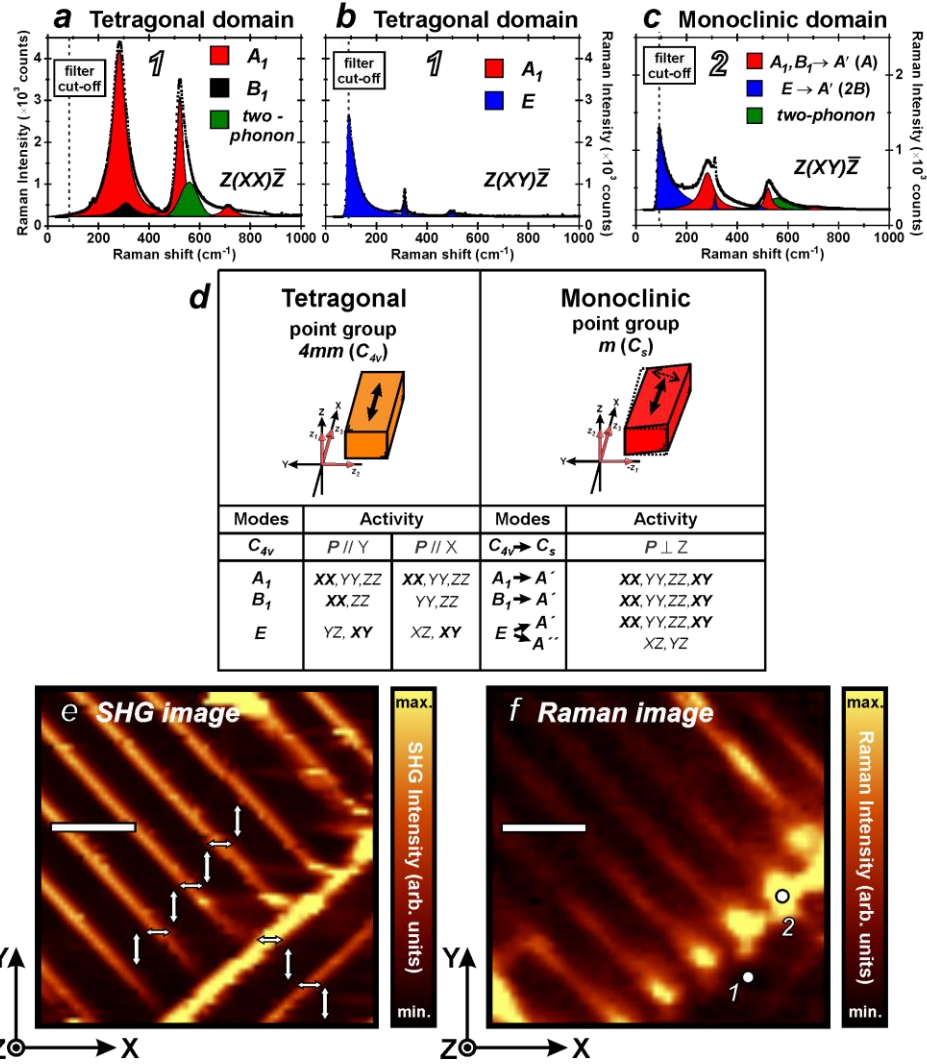
**Supplementary Figure 1.** **a**, Spatial map of the relative polarization rotation angle  $\beta$  at 298 K, corresponding to the domain structure shown in Figure 1c. Here,  $\beta$  is defined as the absolute deviation from the closest nominal  $\langle 100 \rangle$  polarization axis. **b**, Calculated spatial map of the in-plane internal shear stress  $\sigma_{23}$  in the same domain structure. **c**, Corresponding map of the calculated in-plane transverse electric field component  $E_2$ . As illustrated by the strong spatial correlation between  $\beta$ ,  $\sigma_{23}$ , and  $E_2$ , the polarization rotation finds its origin in the combined effect of the local shear stress and transverse electric field, which is consistent with the experimentally found in-plane shear distortion. **d**, Zoomed-in sketch of a slightly bent domain wall, illustrating the mechanism of wall charging upon wall bending (see eq. S9). The domain wall bending angle is given by  $\tau$ , and the surface unit normals for domains 1 and 2 are

indicated by  $\hat{n}_1$  and  $\hat{n}_2$ , respectively. **e**, Polarized optical image (unpolarized incident white light,  $\phi = 0^\circ$ ) of a typical orthogonally twinned multi-domain structure in BaTiO<sub>3</sub>. Scale bar: 2  $\mu\text{m}$ . Domains are delineated by solid black lines for clarity, arrows indicate proposed polarization directions.



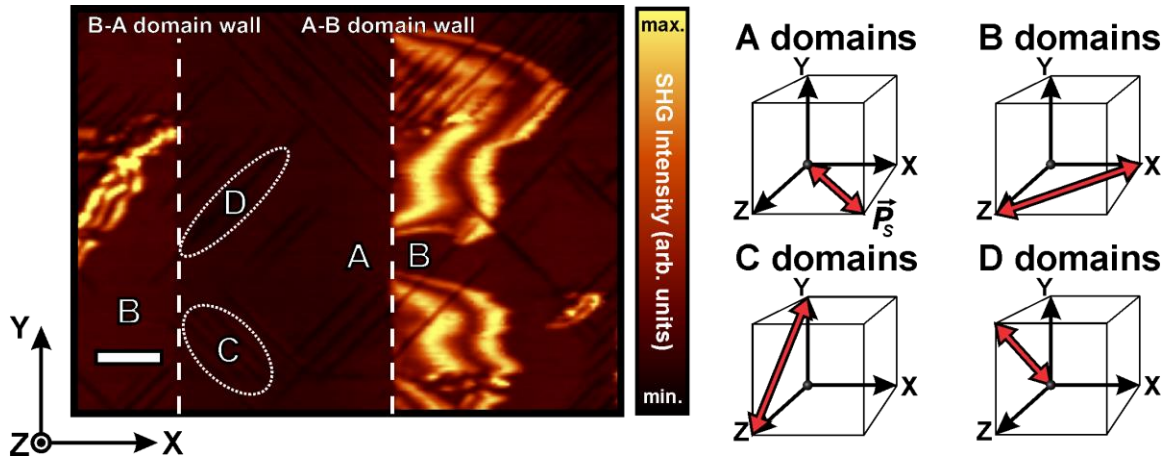
**Supplementary Figure 2.** **a**, Scanning SHG microscopy image ( $I_X^{2\omega}$  with  $E_X^\omega$ ) of an in-plane *a,b*-domain structure in a BaTiO<sub>3</sub> single crystal *without* orthogonal twinning. Scale bar: 8  $\mu\text{m}$ . Ferroelectric polarization ( $\mathbf{P}_\text{s}$ ) axes are marked by double-headed white arrows. **b**, Scanning SHG microscopy image ( $I_Y^{2\omega}$  with  $E_Y^\omega$ ) of an in-plane *a,b*-domain structure in a BaTiO<sub>3</sub> single crystal *with* orthogonal twinning. Scale bar: 12  $\mu\text{m}$ .

**c**, SHG intensity polar plots taken in indicated domains, showing  $I_X^{2\omega}$  and  $I_Y^{2\omega}$  components (radius) versus linear incident light polarization angle (azimuth angle  $\theta$ ). For all polar plots, data points correspond to experiment, with solid lines depicting the corresponding theory fits. Theory for domains 1 and 2 assumed tetragonal 4mm point group symmetry, showing excellent agreement with experiment. By contrast, in domains 3 and 4, neither tetragonal nor orthorhombic models fit experiment. Instead, monoclinic symmetry (point group *m*) is required to match the experimental data.

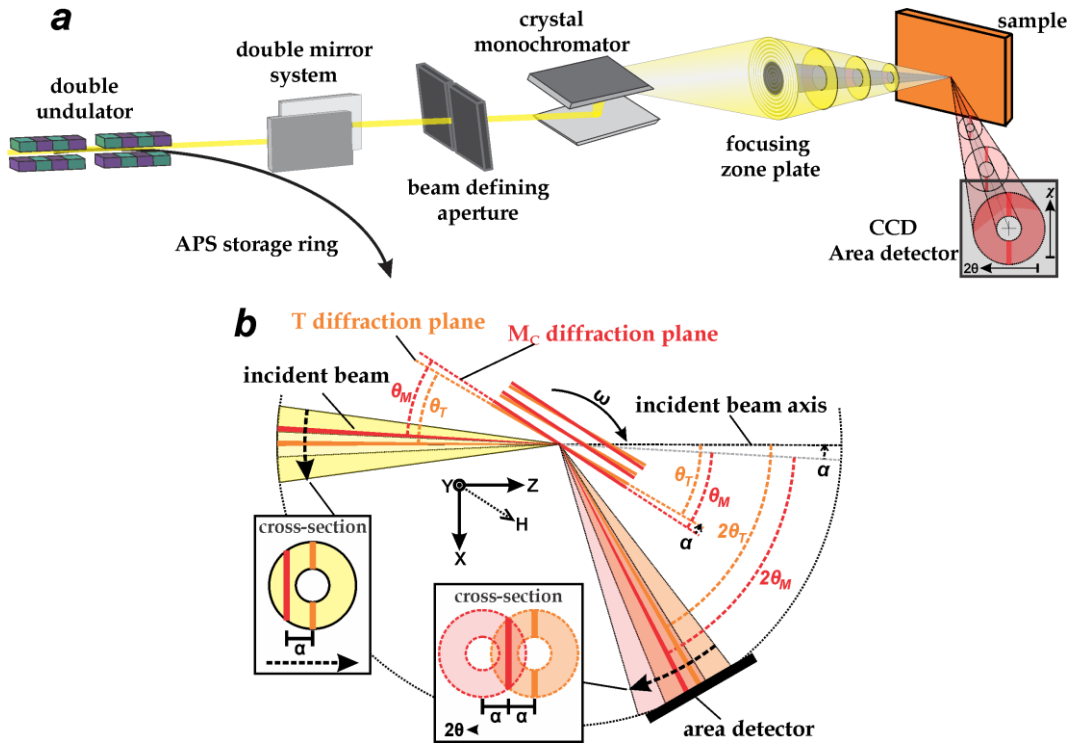


**Supplementary Figure 3.** **a**, Raman spectrum of a tetragonal  $a$ -domain ( $4mm$ , position 1) in an orthogonally twinned multi-domain BaTiO<sub>3</sub> single crystal in parallel ( $Z(XX)\bar{Z}$ ) scattering configuration. **b**, Raman spectrum of the same tetragonal  $a$ -domain (point group  $4mm$ , position 1) in perpendicular ( $Z(XY)\bar{Z}$ ) scattering configuration. **c**, Raman spectrum taken in a monoclinic M<sub>C</sub> domain (point group  $m$ , position 2) in perpendicular ( $Z(XY)\bar{Z}$ ) scattering configuration. For all the spectra shown, Raman mode symmetries<sup>92</sup> are color coded by fitted Lorentzian line shapes as indicated, with dark green line shapes corresponding to two-phonon contributions to the spectra. **d**, Effect of symmetry lowering on Raman selection rules for the point group symmetries considered, in terms of the experimental XYZ coordinate system. Where appropriate, two different in-plane orientations of  $\mathbf{P}_S$  are considered. As clear from the

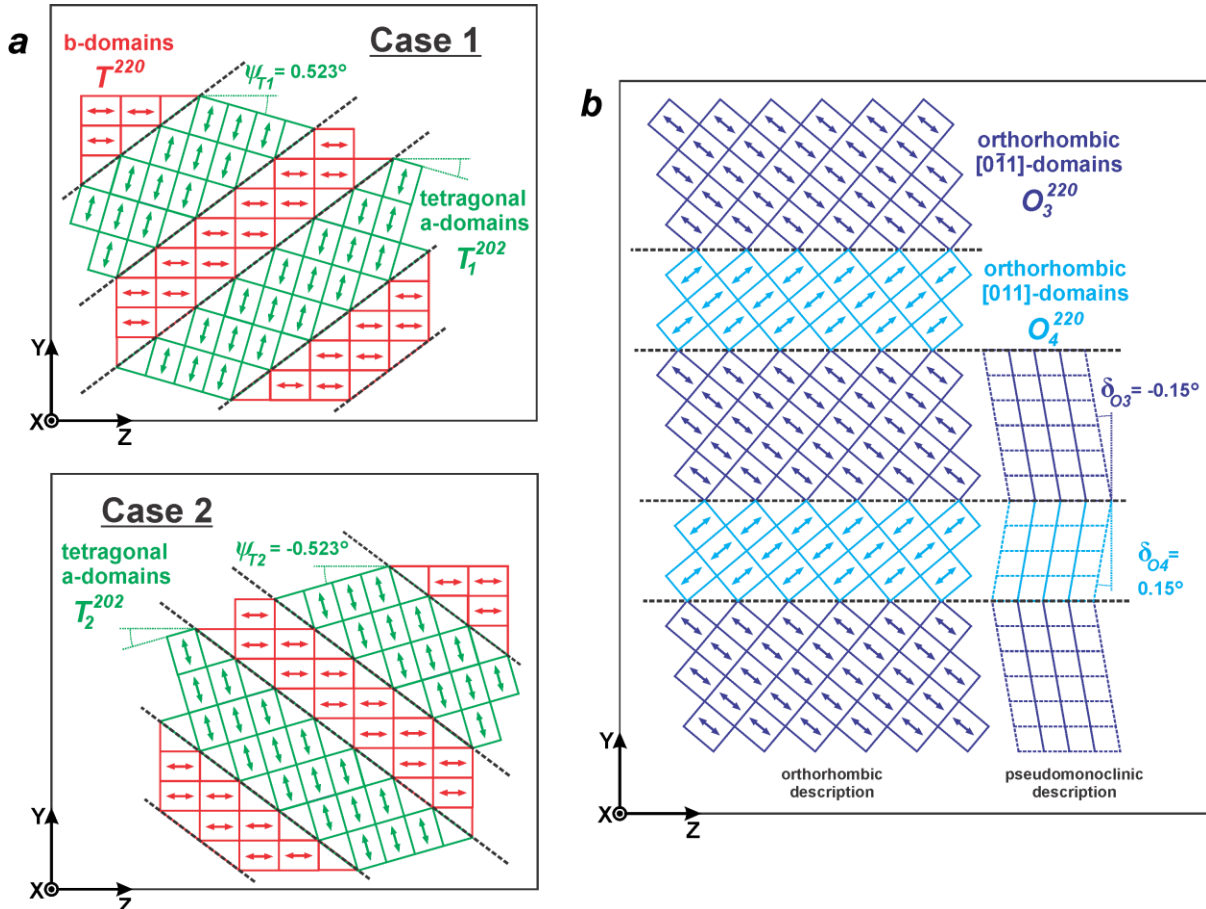
spectra in **a** and **b**, the tetragonal domains adhere to the *4mm* selection rules, with mode frequencies corresponding well to literature values for BaTiO<sub>3</sub><sup>93,94</sup>. Symmetry lowering to a monoclinic M<sub>C</sub> domain however, (point group *m*, mirror plane  $\perp Z$ ;  $P_s \perp Z$ ) reduces the former *A*<sub>1</sub> and *B*<sub>1</sub> modes to *A'* symmetry, making them now additionally active in the  $Z(XY)\bar{Z}$  scattering geometry. Thus, the presence of these modes in the  $Z(XY)\bar{Z}$  spectrum is an adequate “marker” for such an M<sub>C</sub> domain<sup>95</sup>, as illustrated in **c**. **e**, Scanning SHG image ( $I_X^{2\omega}$  with  $E_Y^\omega$ ) of a selected area of an orthogonally twinned multi-domain BaTiO<sub>3</sub> single crystal, where high SHG intensity marks local areas of *m* symmetry. Scale bar: 7  $\mu\text{m}$ . **f**, Corresponding Raman image of the integrated intensity of the  $\approx 530 \text{ cm}^{-1}$  mode in the  $Z(XY)\bar{Z}$  Raman spectrum, which is taken as a marker for monoclinic *m* symmetry. Scale bar: 7  $\mu\text{m}$ . The comparison with **e** shows good agreement between the experimental signatures of *m* symmetry (high intensity in both), thus yielding an independent confirmation of the point group symmetry of the M<sub>C</sub> phase.



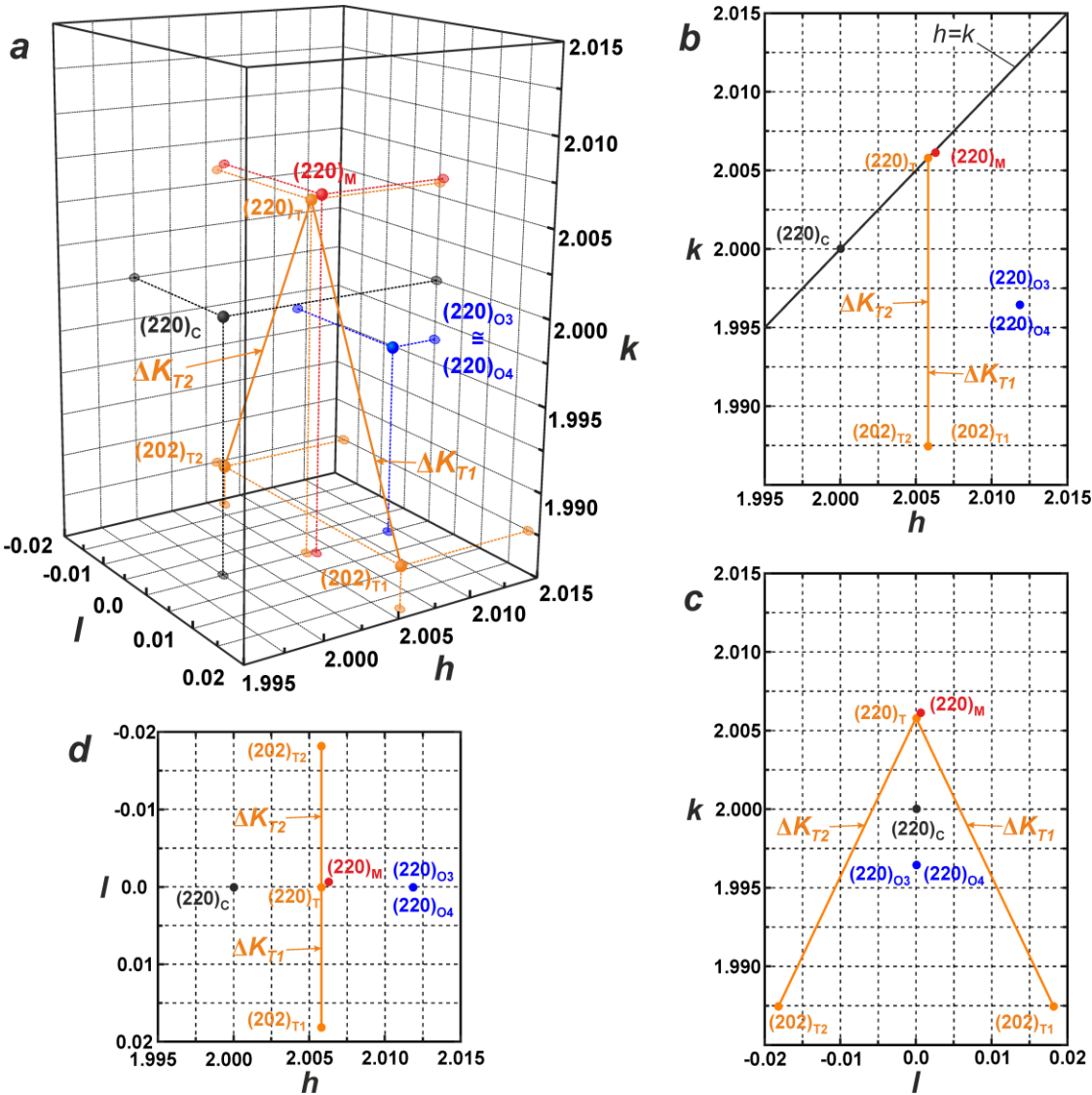
**Supplementary Figure 4.** High-resolution scanning SHG microscopy image ( $I_x^{2\omega}$  with  $E_x^\omega$ ) on densely twinned multi-domain KNbO<sub>3</sub> single crystals at room temperature. The sample surface corresponds to a {100}-cut in pseudocubic coordinates. Scale bar: 5  $\mu\text{m}$ . Ripple features of high SHG intensity, indicative of the induced monoclinic phase in a thermotropic phase boundary, are clearly seen within the orthorhombic domain matrix. Using SHG polarimetry, the polarization in the monoclinic phase was determined to be in the X-Z reference plane. We note that no monoclinic signatures are observed by complementary polarized optical microscopy. Polarization directions with respect to the perovskite pseudocube are sketched on the right for the observed orthorhombic domains, with double-headed arrows indicating the  $P_s$  sign ambiguity in each case.



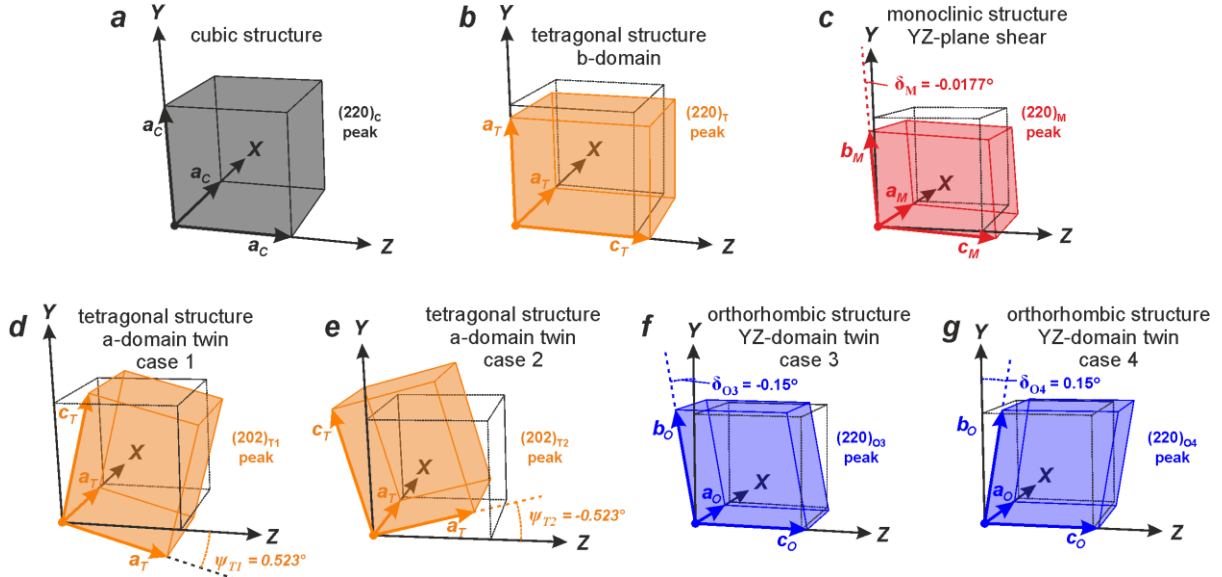
**Supplementary Figure 5.** **a**, Schematic summary of the nano-SXDM technique<sup>44,45</sup>. **b**, Schematic top view of the diffraction process for the sample angle where the T planes diffract the on-axis portion of the incident beam (center diffraction condition of T peak,  $\omega_T = 27.834^\circ$ ). Insets show the schematic cross-sections of the incident and diffracted beams.



**Supplementary Figure 6.** **a**, Schematic sketches of the two types of tetragonal in-plane twinning that could potentially emulate a monoclinic shear in the YZ plane. The distinct cases 1 and 2 show the relative orientations of hypothetical *a*-domain twins with respect to that of the reference *b*-domains. **b**, Schematic sketch of the only type of orthorhombic in-plane twinning that could potentially emulate a monoclinic shear in the YZ plane. The twinning structure is drawn with both the conventional orthorhombic and the pseudo-monoclinic description of the unit cell<sup>29</sup>. In each sketch, the plane of the figure corresponds to the crystal surface. Unit cell distortions are drawn exaggerated for clarity.



**Supplementary Figure 7.** **a**, Three-dimensional plot of the relevant diffractions peak positions (colored solid spheres) in reciprocal space. Solid lines  $\Delta K_i$  indicate coarse twin peak splitting vectors, and represent the lever rules for the reciprocal space position of potential adaptive superlattice peaks. Dashed lines mark projections in the  $hk$ -,  $kl$ -, and  $hl$ -planes, which are individually plotted in panels **b**, **c**, and **d**, respectively. Axes are scaled by the reciprocal lattice unit,  $1.566 \text{ \AA}^{-1}$ , defined through the lattice constant of cubic BaTiO<sub>3</sub> at 450 K<sup>28</sup>.



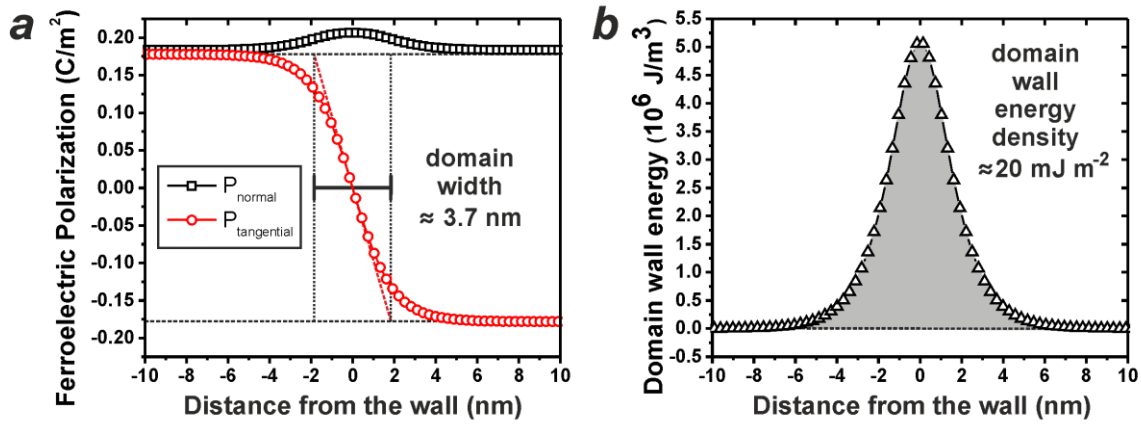
**Supplementary Figure 8.** Panels **a** through **g** sketch the relative geometric orientations of the unit cells relevant in considering a potential adaptive superlattice, with respect to that of the reference tetragonal *b*-domain (panel **b**). Corresponding reciprocal lattice vectors in the *XYZ* reference frame are provided in Supplementary Table 1.

**Supplementary Table 1.** Structural parameters of relevant domains.

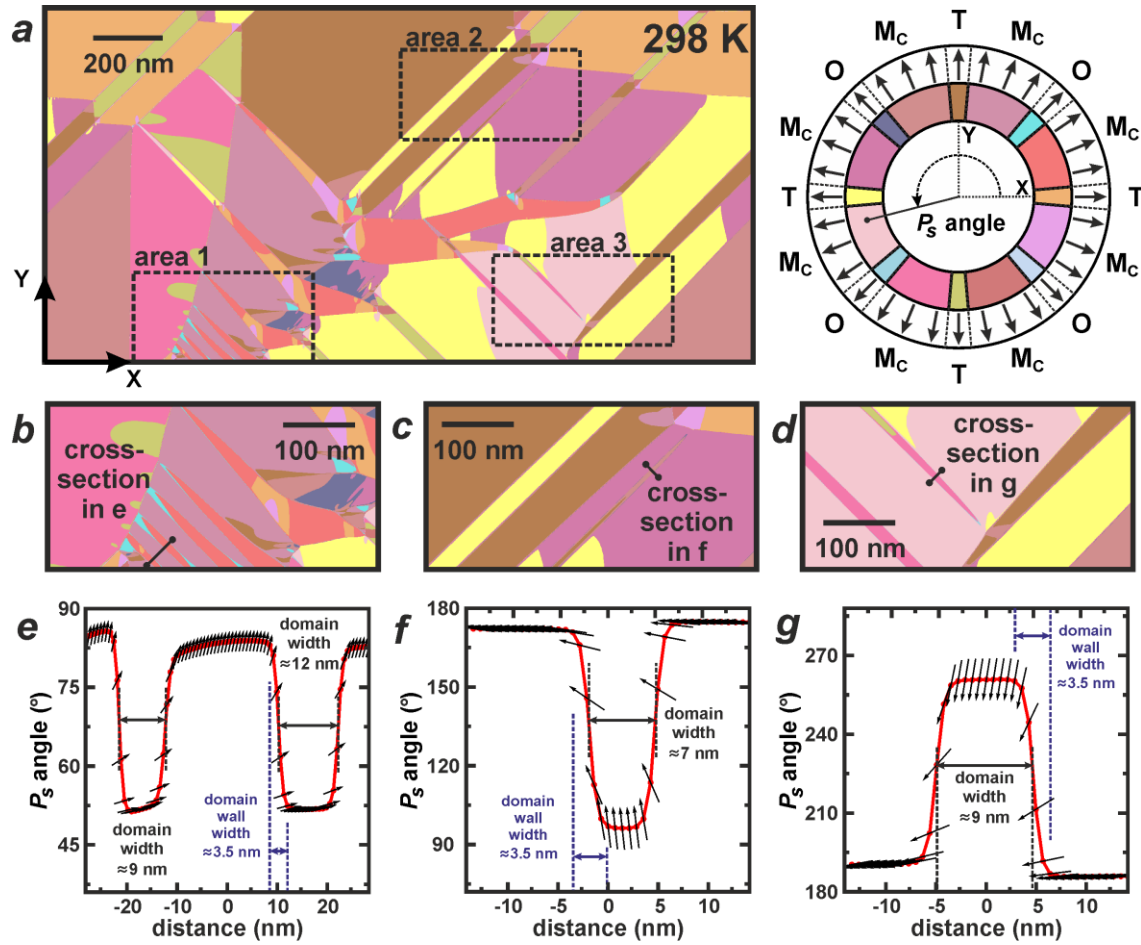
	C <sup>28</sup>	T	Mc	T1	T2	O3 <sup>29</sup>	O4 <sup>29</sup>
<b>Lattice constants</b>	$a_C = 4.011 \text{ \AA}$	$a_T = 3.9994 \text{ \AA}$ $b_T = 3.9988 \text{ \AA}$ $c_T = 4.0361 \text{ \AA}$ $\delta_M = -0.0177^\circ$	$a_M = 3.9984 \text{ \AA}$ $b_M = 3.9988 \text{ \AA}$ $c_M = 4.0361 \text{ \AA}$ $\psi_{T1} = 0.523^\circ$	$a_T = 3.9994 \text{ \AA}$ $c_T = 4.0361 \text{ \AA}$ $\psi_{T2} = -0.523^\circ$	$a_T = 3.9994 \text{ \AA}$ $c_T = 4.0361 \text{ \AA}$ $\psi_{T2} = -0.523^\circ$	$a_O^\dagger = 3.9874 \text{ \AA}$ $b_O^\dagger = 4.0812 \text{ \AA}$ $c_O^\dagger = 4.0812 \text{ \AA}$ $\delta_{O3}^\dagger = -0.15^\circ$	$a_O^\dagger = 3.9874 \text{ \AA}$ $b_O^\dagger = 4.0812 \text{ \AA}$ $c_O^\dagger = 4.0812 \text{ \AA}$ $\delta_{O4}^\dagger = 0.15^\circ$
<b>Sketch</b>	Supp. Fig. 8a	Supp. Fig. 8b	Supp. Fig. 8c	Supp. Fig. 8d	Supp. Fig. 8e	Supp. Fig. 8f	Supp. Fig. 8g
<b><math>h^*</math></b>	2.000	2.0058	2.0063	2.0058	2.0058	2.0118	2.0118
<b><math>k^*</math></b>	2.000	2.0058	2.0061	1.9875	1.9875	1.9964	1.9964
<b><math>l^*</math></b>	0	0	0.0006	0.0182	-0.0182	0	0

<sup>†</sup>pseudo-monoclinic description of the orthorhombic unit cell<sup>29</sup>

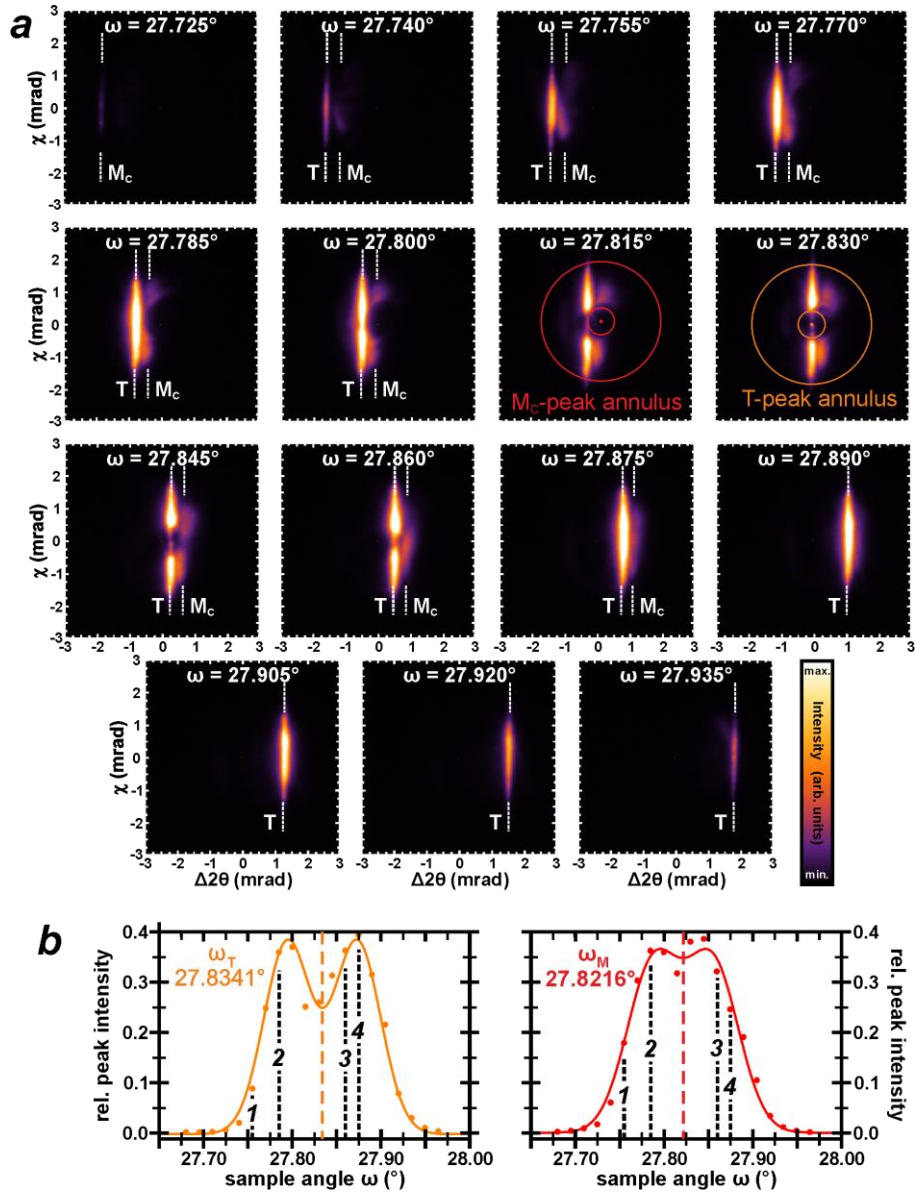
<sup>‡</sup> Reciprocal space coordinates of relevant diffraction peaks in the reference frame of the tetragonal *b*-domain (in cubic reciprocal lattice units<sup>28</sup>; 1.566 Å<sup>-1</sup>)



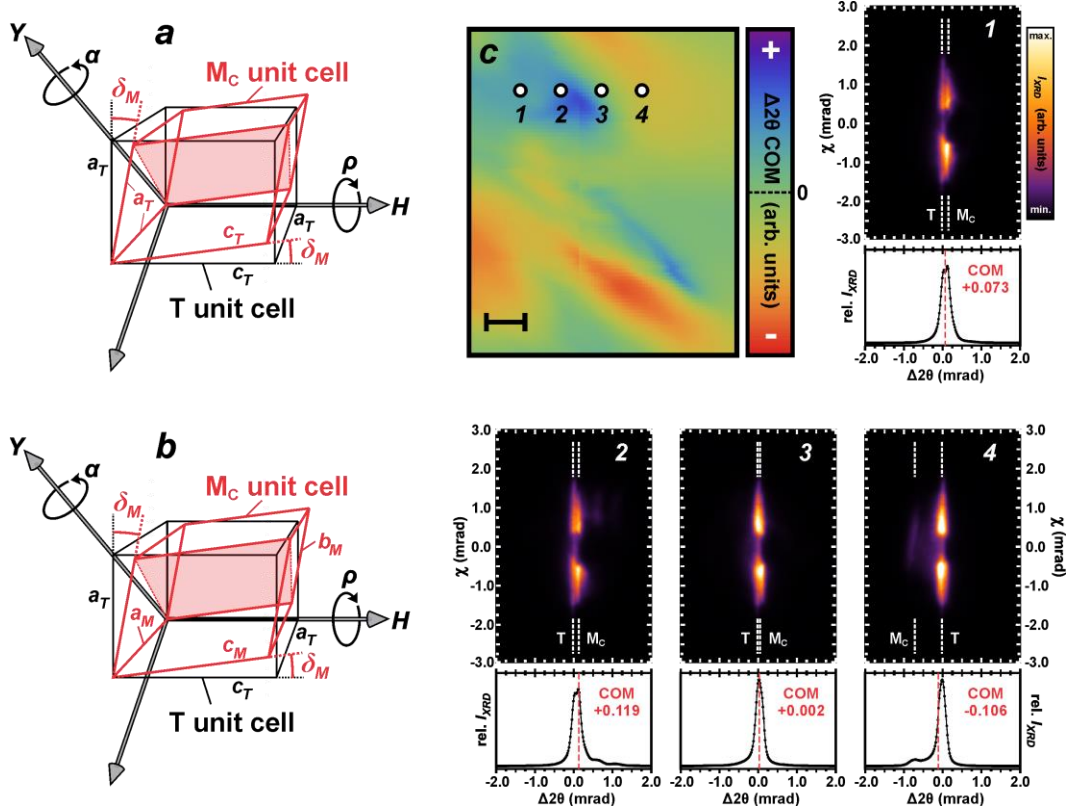
**Supplementary Figure 9.** **a**, Phase-field calculated components of the ferroelectric polarization across a  $90^\circ$  head-to-tail wall in BaTiO<sub>3</sub> at 298 K. **b**, Corresponding wall energy versus position, defined as the local free energy of the  $90^\circ$  head-to-tail domain wall minus that of a single equilibrated tetragonal domain. The area under this curve gives the domain wall energy density.



**Supplementary Figure 10.** **a**, High-resolution phase-field simulation of an orthogonally-twinned BaTiO<sub>3</sub> domain structure at 298 K. Panels **b** through **d** show zoom-ins on indicated areas 1 through 3, respectively. The phase classification in terms of discrete ferroelectric polarization ( $\mathbf{P}_S$ ) orientation ranges is shown on the top right. Panels **e** through **g** plot cross-sectional traces across the smallest domains observed. Corresponding domain and domain wall widths are indicated. Black arrows indicate local polarization vectors  $\mathbf{P}_S$ .

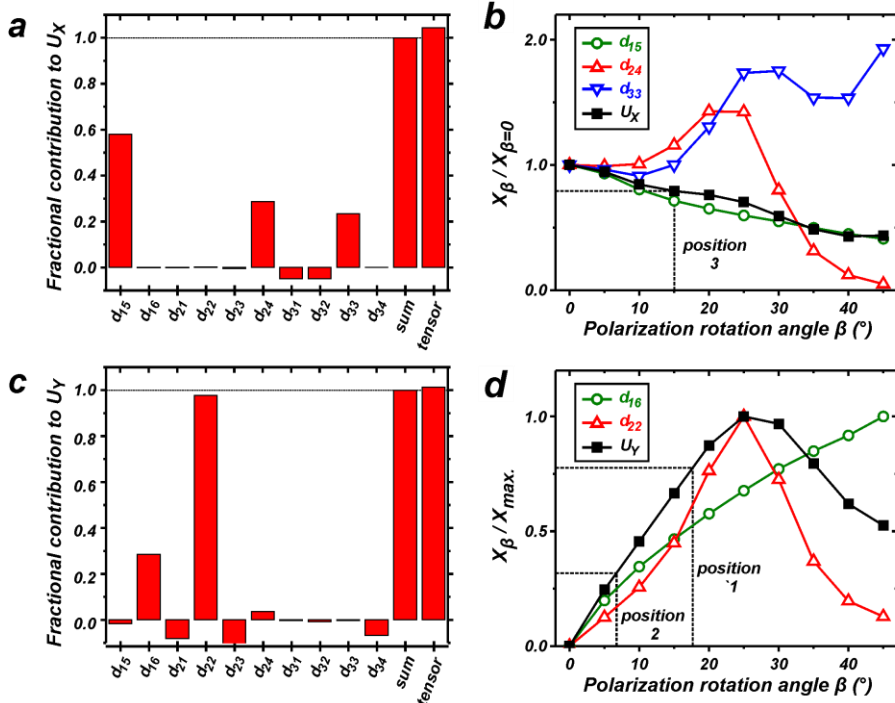


**Supplementary Figure 11.** **a**, Background-subtracted, normalized 2D diffraction images taken at indicated sample angles in the SXDM rocking curve. **b**, Corresponding integrated peak intensity versus sample angle ( $\omega$ ) for both T (left) and  $M_c$  diffraction (right). The experimental data points were fitted with a pair of twin Gaussian line shapes (solid lines) to extract the center diffraction conditions for the two peaks (colored lines).



**Supplementary Figure 12.** **a**, Schematic geometrical model of a pure shear distortion of the tetragonal unit cell (edge lengths of the M<sub>C</sub> parallelepiped equal to the tetragonal lattice constants). **b**, Schematic geometrical model of a simultaneous shear distortion and change in lattice constants. In both **a** and **b**, the orientation of the (220) diffraction planes of the M<sub>C</sub> phase is indicated by the filled red shape (only one plane is shown for clarity). Sample surface is in the (a<sub>T</sub>, c<sub>T</sub>) -plane. Directions of relative rotations relevant for (220) diffraction are indicated ( $\alpha$  and  $\rho$  impacting  $2\theta$  and  $\chi$ , respectively), with the Y-axis as defined in Supplementary Figure 5b and the H-axis equivalent to the intersection of the tetragonal (220) plane and the XZ-plane. **c**, Aspect-ratio corrected high-resolution spatial map (80 nm step size) of the relative  $2\theta$  COM of the (220) diffraction signal. Scale bar: 1  $\mu\text{m}$ . For reference,  $\Delta 2\theta = 0$  refers to  $2\theta = 51.9869^\circ$ , which corresponds to the averaged  $2\theta$  COM value of the T-peak. Background-subtracted, normalized 2D diffraction images and corresponding normalized integrated XRD intensity plots ( $I_{XRD}(2\theta)$ ) at the indicated positions are shown on the right/bottom. Here, white dashed lines (top) indicate positions of the T and M<sub>C</sub> peaks, with dashed red lines (bottom) indicating the  $2\theta$  COM values of the total (T+ M<sub>C</sub>)

diffraction used to generate the spatial map. The  $M_C$  peak-shape variation is a consequence of the annular cross-section of the incident beam<sup>44,45</sup>.



**Supplementary Figure 13.** **a**, Fractional contributions of each piezoelectric  $d_{ij}$  coefficient to  $U_X$ , for a monoclinic domain in which  $\beta = 5^\circ$ . Fractional contributions are calculated by having all but the  $d_{ij}$  in question set to zero in the FEM simulation. The bar named “tensor” corresponds to the FEM simulation with the full tensor. Its excellent agreement with the sum value demonstrates the validity of this approach. Relative contributions are qualitatively similar for all  $\beta$ . **b**, Dependence of  $d_{15}$ ,  $d_{24}$ ,  $d_{33}$ , and  $U_X$  on the polarization rotation angle  $\beta$ , normalized to the corresponding FEM calculated value for  $\beta = 0$ . For reference,  $d_{15}^{\beta=0^\circ} = d_{24}^{\beta=0^\circ} = 325 \text{ pm V}^{-1}$ ,  $d_{33}^{\beta=0^\circ} = 56 \text{ pm V}^{-1}$  and  $U_X^{\beta=0^\circ} = -146 \text{ pm}$  (at a field of +1.0 V). Dashed lines indicate the estimation of the polarization rotation angle corresponding to position 3 in Figure 4a. **c**, Fractional contributions of each piezoelectric  $d_{ij}$  coefficient to  $U_Y$ , for a monoclinic domain in which  $\beta = 5^\circ$ . **d**, Dependence of  $d_{16}$ ,  $d_{22}$  and  $U_Y$  on the polarization rotation angle  $\beta$ , normalized to the corresponding maximum value in the  $\beta$ -range. For reference,  $d_{16}^{\beta=45^\circ} = 133 \text{ pm V}^{-1}$ ,  $d_{22}^{\beta=25^\circ} = 842 \text{ pm V}^{-1}$

<sup>1</sup> and  $U_Y^{\beta=25^\circ} = -135$  pm (at a field of +1.0 V). Dashed lines indicate the estimation of the polarization rotation angles corresponding to positions 1 and 2 in Figure 4a.